HOT DEFORMATION OF A MICROALLOYED STEEL

Javier Ruete

INDEX

1. INTRODUCTION

The hot forming processes of materials constitute a very important step in the manufacture of mechanical components [1]. The hot deformation not only provides the desired geometry but also the mechanical and microstructural features.

The design of hot forming processes consists in achieving the final appropriate physical and mechanical properties of the material and the selection of the control parameters of the deformation process.

Several authors as for example[2-5] have extensively studied the strain, the strain rate, the temperature and the microstructural effect in the flow behavior of metals during the deformation process, such as Frost and Ashby [4] with the deformation maps and Raj [6] with the processing maps. These maps are calculated with equations which relate the flow stress with the temperature, the strain rate and the starting microstructure and they can be used to predict the optimal parameters of deformation.

There are different models to calculate deformation maps. For some materials, one kind of deformation map fits very well but for other materials the same model does not fit.

The aim of the project is the study of the deformation behaviour of microalloyed steel by means of processing maps and microstructural characterization. Furthermore a comparison of different types of processing maps is presented.

2. STATE OF ART

2.1. FORMABILITY

Formability is the capacity of a material to deform plastically without damage. It can be considered to consist of two independent parts: a) intrinsic formability; which depends on the constituent behavior of the material, and b) state-of-stress: SOS which depends on the nature of the stress applied and the geometry form in the deformed area [1].

To avoid the formation of faults that do not support formability like shear bands, boundary cavities, triple junction cracking, and to obtain final products which have controlled microstructure and properties controlled, it is necessary to have a global knowledge of the parameters that can affect the formability during the forming process [1].

2.2. DEFORMATION MAPS

A material can be deformed according to several deformation mechanisms. In a certain interval of temperatures and strain rates, one deformation mechanisms will prevail. All of them work at the same time and the faster one can usually control the flow behaviour. A way

to determine the process that occurs during the deformation is the use of deformation maps [1].

2.2.1. ASHBY-FROST DEFORMATION MAPS

Each deformation mechanism can be described by an equation that relates the shear strain rate, the shear stress, the absolute temperature and the microstructure. Ashby and Frost designed deformation maps that depicted the normalized stress multiplied for the shear modulus opposite of homologues temperature ($T/T_{melting}$) pointing out in each strain rate, which was the active mechanism. These maps provide information about the deformation mechanism that is expected to be found in conditions of a thermodynamic process at strain rates smaller than 10^{-3} s^{-1} [1].

2.2.2. RAJ DEFORMATION MAPS

Raj [6] extended the concept of the deformation maps considering two important mechanisms of damage that are relevant to the deformation. One is the cavities formation at hard particles in a soft matrix. These particles do not deform but localization strain occurs at the surrounding matrix which can lead in pore formation. This mechanism occurs at lower temperature and higher strain rates. [1].

When the temperature is high, the velocity of the cavities formation is slow because of the low hardness speed due to recovery. Thereby, Raj [6] established the minimum conditions (combination of temperature and strain rate) for the cavities formation near the hard particles.

The second damage mechanism is the triple junction cracking, the crack is formed at in the grain boundary to decrease the stress concentration due to the gliding of the grains boundary at high temperatures and low strain rates.

Additionally, when the strain rates are high, flow localization can take place by local increment of the temperature due to adiabatic flow behaviour [7].

The "safe" combination of the processing parameters is given when damage never happen.

2.3. DYNAMIC MODELING OF THE MATERIAL BEHAVIOUR

2.3.1. BASIC CONCEPTS

The basic notions for the construction of the power dissipation maps is the dynamic materials model (DMM) developed by Prasad et al. [8] In this model, the workpiece formed at high temperature is considered as the only part of the whole system of the process that is able to dissipate energy. The constitutive equation is a phenomenological relation that describes the flow stress change with the deformation parameters. For a given temperature and strain rate, it is assumed that the constitutive dynamic equation follows a potential law:

$$\sigma \cdot K \cdot \dot{\varepsilon}^{m} \qquad (1)$$

4

Where K is a material constant, *m* is the strain rate sensitivity, σ is the stress and $\dot{\varepsilon}$ is the strain rate. In hot deformation of pure metals [7], *m* is independent of the temperature and the strain rate; but in the case of alloys, it has been demonstrated that *m* changes with the temperature and the strain rate.

For the DMM there are some general principles. It is considered that the material has the following characteristics [9].

(1) Dissipative: During the hot deformation the material only dissipates energy and therefore there is not significant energy stored.

(2) *Dynamic*: During hot deformation the constituent behaviour of the material at a given temperature depends mainly on the strain rate and to a lesser way of the strain.

(3) *Non-linear*: The behaviour of the material to the application of different variables like strain, strain rate and temperature is nonlinear.

(4) *Far from equilibrium*: If the strain is not being applied with infinitesimally small increments in the material that undergoes at large plastic flow at high temperatures, it is far from the equilibrium.

(5) *Irreversible*: The extreme principles of irreversible thermodynamics from Ziegler are applicable to large plastic flow.

The total imposed power *P* can be calculated as it is shown in equation 2.

$$P = \sigma \cdot \dot{\varepsilon} \ = \int_0^{\dot{\varepsilon}} \sigma \cdot d\dot{\varepsilon} + \int_0^{\sigma} \dot{\varepsilon} \cdot d\sigma = G + J \qquad (2)$$

For understanding the physic sense of *G* and *J*, the microscopic process of plastic deformation should be considered. Plastic flow occurs for crystallographic sliding, that results of the dislocation motions in their slide planes undergoing a shear stress τ. The τ action increases the kinetic and potential energy. A big part of the potential energy is almost instantly transformed in kinetic energy. However the kinetic energy provided by the plastic flow is transformed into heat. The most of these transformations is dissipated by heat and it is represented by the dissipator *G* and the rest of the energy is stored like faults [1].

Other microscopic processes which annihilate dislocations and dissipate energy can exist as well. All of these metallurgical phenomena contribute to the energy dissipation but in a lower proportion than the power dissipator content, and they represent the complementary function, J: the dissipator co-content. The conclusion is that at either instant the energy dissipation occurs through heat (the dissipator content, *G*) or structural changes (the dissipator co-content, *J*) [1].

2.3.2.   CO-CONTENT J EVALUATION

The power partitioning between *G* and *J* is controlled by the constitutive flow behavior of the material and is decided by the strain rate sensitivity (m) and it is usually varying with the temperature and the strain. The power partitioning is given by [10]:

$$\frac{dJ}{dG} = \frac{\dot{\varepsilon} \cdot d\sigma}{\sigma \cdot d\dot{\varepsilon}} = \frac{\dot{\varepsilon} \cdot \sigma \cdot dln\sigma}{\sigma \cdot \varepsilon \cdot d\dot{ln\varepsilon}} = \frac{\Delta log\sigma}{\Delta log\dot{\varepsilon}} \equiv m \qquad (3)$$

In the extreme case, J can be equal to G, because the dislocations cannot be annihilated at higher velocity than they are created. This is the ideal case of a linear dissipator where $m = 1$ and $J = J_{max} = G_{min} = 0.5\ P$ and the half of the power is dissipated as plastic flow and the other half is dissipated in terms of heat. On the other extreme $m = 0$ and $J = 0$ and the workpiece does not dissipate power through metallurgical processes. The stable plastic flow occurs among the two extremes, $m = 1$ and $m = 0$ [1].

The co-content J can be explicitly evaluated from the integral [11]:

$$J = \int_0^\sigma \dot{\varepsilon}\ d\sigma \qquad (4)$$

In materials that have a complex microstructure or two-phase alloys, the dynamic metallurgical processes which contribute to the power dissipation during hot deformation, occur simultaneously and/or interactively. Thereby, the result given by J will be the global result of these interactions. The metallurgical processes, such as dynamic recovery, dynamic recrystallization, wedge cracking, dissolution or particle growth , induced phase transformation by deformation or dynamic precipitation, contribute for a change in the power dissipated J [7].

2.3.3. THE EFFICIENCY OF POWER DISSIPATION

The maximum velocity for annihilating dislocations can be at most equal the generation velocity of these, so the power dissipation through the co-content J can be normalized with the linear dissipator [7].

$$\left[m = 1\ ; J_{max} = \left(\frac{\sigma \cdot \dot{\varepsilon}}{2} \right) \right] \qquad (5)$$

A dimensionless parameter called efficiency of power dissipation (η) can be calculated as follows [10]:

$$\eta = \frac{J}{J_{max}} = \frac{2\ m}{m+1} \qquad (6)$$

The variation of η with the temperature and strain rate represents the features of the power dissipation through the microstructural changes in the workpiece formed and constitutes the processing map. The map can show several domains that can be correlated with specifics microstructural mechanisms [7].

2.3.4. DETERMINATION OF THE INSTABILITY FLOW AREAS

Ziegler considerate some extreme irreversible thermodynamic principles applied to the continuum mechanic of plastic flow deformations.

Ziegler demonstrated that instable flow occurs if the differential quotient satisfies the inequality [12]:

$$\frac{dD}{d\dot{\varepsilon}} < \frac{D}{\dot{\varepsilon}} \qquad (7)$$

Where *D* is the dissipation function which represents the constitutive behavior of the material and is defined by:

$$D = \theta \frac{dS}{dt} = \geq 0 \qquad (8)$$

Where θ the temperature and S is the entropy.

Krumar and Prasad applied the equations shown before for developing a criterion to predict instabilities during the formability of a material. As *J* is the responsible of the power dissipation through metallurgical processes, the dissipation function related with metallurgical stability is represented by *J*. With replacing *D* for *J* in the equation (8), the conditions for the metallurgical instability at constant deformation and constant temperature can be obtained.

$$\frac{dJ}{d\dot{\varepsilon}} < \frac{J}{\dot{\varepsilon}} \qquad (9)$$

Replacing *J= (m/m+1)·σ·ε̇* in the equation before, the dimensionless parameter of microstructural instability is obtained [8].

$$\xi(\dot{\varepsilon}) = \frac{dln[{}^m/_{m+1}]}{dln\dot{\varepsilon}} + m < 0 \qquad (10)$$

Therefore, the variation of ξ with the temperature and the strain rate constitutes the instability map that can be superimposed to the dissipation power map obtaining the processing map. The instability map delineates the instability areas where the parameter ξ is negative and therefore, these will be areas to avoid in the forming process.

2.3.5. MODIFIED DMM

The DMM was re-analyzed by Murty and Rao [9], who demonstrated that if *m* varies with $\dot{\varepsilon}$ and *T* as in many engineering alloys, the flow stress does not obey one power law, and hence, the evaluation of *J = mP/(1 +m)* is erroneous.

As the experimental data usually are not available up to a minimum strain rate, the integral to evaluate *G* can be expressed by [8]:

$$G = \int_0^{\dot{\varepsilon}_{min}} \sigma d\dot{\varepsilon} + \int_{\dot{\varepsilon}_{min}}^{\dot{\varepsilon}} \sigma \, d\dot{\varepsilon} = \left[\frac{\sigma \dot{\varepsilon}}{m+1}\right]_{\dot{\varepsilon}=\dot{\varepsilon}_{min}} + \int_{\dot{\varepsilon}_{min}}^{\dot{\varepsilon}} \sigma \, d\dot{\varepsilon} \qquad (11)$$

The value of *m* for the first integral is estimated as the derivative of the curve $\log \sigma - \log \dot{\varepsilon}$.

The instability condition in the modified DMM is expressed by [13]:

$$K = \frac{2\,m}{\eta} - 1 < 0 \qquad (12)$$

7

According to [14], there is another parameter to calculate the instability. This parameter is k_j and its equation is:

$$k_j = \frac{\partial lnJ}{\partial ln\varepsilon} - 1 \qquad (13)$$

2.4. MICROSTRUCTURE EVOLUTION DURING HOT DEFORMATION

The stored energy due to the accumulated dislocations during cold deformation is generally lowered by three processes: recovery, recrystallization and grain growth [15]. Recovery is a process where annihilation and rearrangement of the dislocations occurs. Recrystallization involves the formation of new grains free of dislocations. The grains grow on the old deformed grains, resulting a new structure with low dislocation density. Grain growth is the process when the grains coarsen and the grain boundary area is reduced.

Recovery and recrystallization can take place during and after deformation and to distinguish them they are called dynamic and static recrystallization, respectively. If the recrystallization after deformation is preceded by dynamic recrystallization it is called metadynamic [16]. The flow curve is dependent on the conditions of the deformation, such as temperature, T, and strain rate, $d\varepsilon/dt$, which can be expressed by the Zener-Hollomon parameter [17].

$$Z = A\,\dot{\varepsilon}exp\left(\frac{Q}{R\,T}\right) \qquad (14)$$

Q is the apparent activation energy for deformation, R is the gas constant, 8.314 J ·mol $^{-1}$K $^{-1}$ and A is a material constant.

2.4.1. THE GRAIN STRUCTURE

The kinetics of the recrystallization and grain growth depends on the migration of grain boundaries. Grain boundaries are regions of considerable atomic misfit and act as strong barriers to the dislocation motion [18]. A grain boundary is a boundary that separates regions of different crystallographic orientations. The misorientation between two grains is the smallest rotation required to make the two crystals coincide [19]. A schematic picture of a grain boundary is shown in Figure 1. Five macroscopic degrees of freedom are needed to define the geometry of a boundary. In Figure 1, AB represents a boundary plane and the overall geometry of the boundary is defined by the orientation of this plane with respect to one of the two crystals (two degrees of freedom) and by the angle θ (three degrees of freedom).
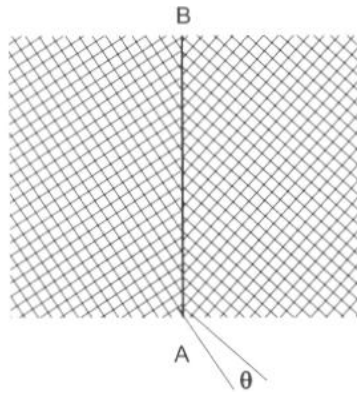
Fig.1. Schematic presentation of a grain boundary between two crystals misoriented by an angle θ, from Humphreys and Hatherly [19].

Grain boundaries are usually separated into the categories of low and high angle grain boundaries which depend on the size of the misorientation [19]. Low angle grain boundaries (LAGB) or subgrain boundaries are boundaries misoriented by an angle less than 10-15°. Meanwhile high angle grain boundaries (HAGB) are boundaries misoriented by an angle higher than 10-15°. The definition of grains with low angle boundaries and high angle boundaries play an important role in the description of recrystallization [20].

2.4.2. DISLOCATION GENERATION AND RECOVERY

Almost all of the applied work during hot deformation turns into heat and only a small part remains as stored energy (~1%) [19]. Essentially the increase in stored energy is due to the accumulation of dislocations which is caused by both tangling of existing dislocations and the generation of new ones. The energy is also raised by the increase of grain boundary area. The stored energy in the material is the driving force for recovery and recrystallization [20].

Recovery of the material is a process that occurs prior to recrystallization and is primarily due to changes in the dislocation structure. During recovery, the dislocations rearrange in configurations of lower energy. Recovery develops by: formation of cells, annihilation of dislocations within cells, formation of subgrains and subgrain growth [19], as can be seen in Fig.2.

(a) Dislocation tangles   (b) Cell formation   (c) Annihilation of dislocations within cells

(d) Subgrain formation   (e) Subgrain growth
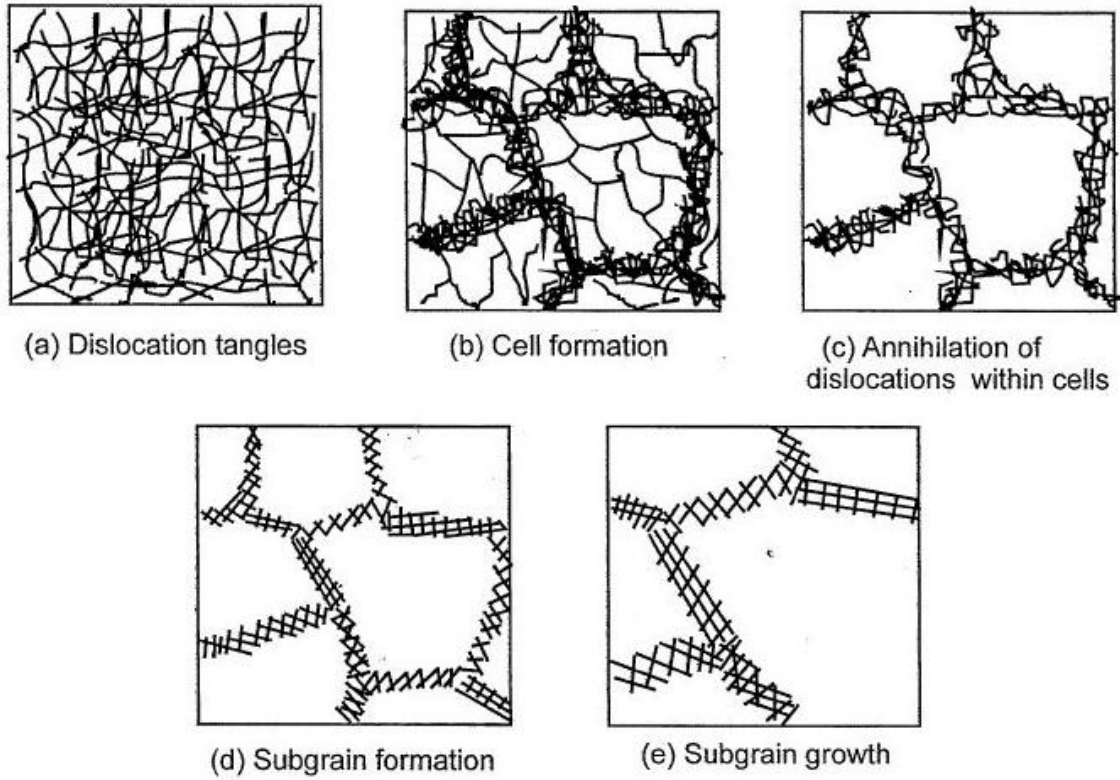
Fig.2. The stages of recovery where first cells are formed due to the rearrangement of dislocations and then subgrains are formed and grow due to annihilation of dislocations, from Humphreys and Hatherly [18].

During hot deformation, dislocation accumulation due to deformation and annihilation and rearrangement of dislocations due to dynamic recovery occurs simultaneously. The evolution of dislocations during hot deformation can be separated in two parts – dislocation generation and dislocation recovery [20].

$$\frac{d\rho}{dt} = \frac{d\rho_{gen}}{dt} - \frac{d\rho_{recovery}}{dt} \qquad (14)$$

ρ_{gen} is the generated dislocation density and $\rho_{recovery}$ is the annihilated dislocation density. When dynamic recovery is the main form of restoration that occurs in the material, the flow-stress in a stress-strain curve reaches a plateau and then holds a steady-state flow-stress. This is because both, the rates of recovery and work hardening reach a dynamic equilibrium [20].

10

2.4.3. RECRYSTALLIZATION AND GRAIN GROWTH

The definition of recrystallization according to Doherty et al. [21] is "the formation of a newgrain structure in a deformed material by the formation and migration of high angle grain boundaries driven by the stored energy of deformation". Consequently, recrystallization is a process where new dislocation-free grains grow on the expense of the old deformed grains, building a new structure with low dislocation density as a result. The process is divided into nucleation of new grains and growth of them.

Recrystallization is a fast process and new grains grow from small regions which are already present in the structure, like subgrains or cells. The subgrains must have an energy advantage, and a larger size to be able to grow rather than shrink and vanish. Hence, for the recrystallization to take place, a critical subgrain size has to be reached. This critical size is large in comparison with the mean subgrain size, which means that it can only be reached by abnormal growth [20].

There is a general assumption that both subgrain coarsening and nucleation of recrystallization from pre-existing subgrains are controlled by the migration of low angle grain boundaries. Subgrain coarsening in regions of large orientation gradient is believed to be a mechanism by which recrystallization emerges [22]. When an orientation gradient is present in the deformed and recovered material, the subgrains will grow more rapidly than those in an environment where there is no orientation gradient. When the growing of the subgrains is faster, it is obtained more misorientation, which results in the creation of a high angle grain boundary and consequently a nucleus [20].

Hence, for static recrystallization to take place a critical subgrain size has to be reached and the misorientation has to be high enough, i.e. it has to be a high angle grain boundary. Preferable nucleation sites for recrystallization are grain boundaries [19, 23] and the new grains form a "necklace" around the deformed grain, see Fig. 3. When the grains are very large, intergranular nucleation occurs where new grains nucleate at the interior of the grains as well and not only at the prior deformed austenite grain boundaries [19], see Fig. 3.

Prior grain boundary
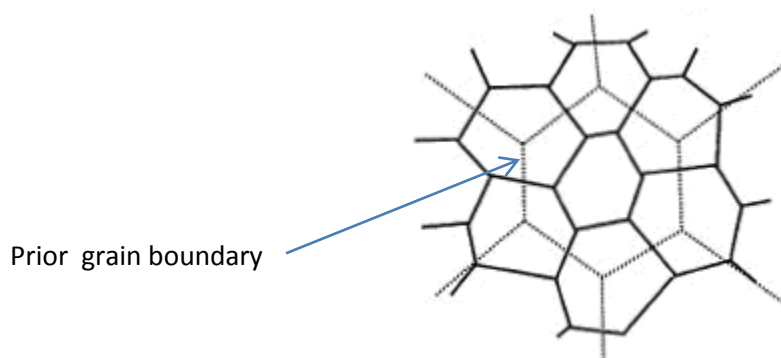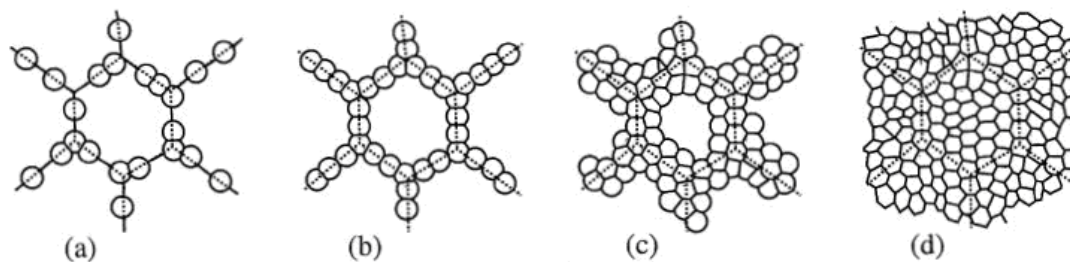
Fig.3. A schematic picture of the development of recrystallizing grains, where the initial grain size is large in comparison with the new recrystallized grains. The dotted lines illustrate prior grain boundaries and the continuous lines show new recrystallized grains. From Humphreys and Hatherly [18].

The recrystallized grain size is reduced when larger deformations are applied. Larger deformations give smaller subgrains and thereby increases the number of nuclei for recrystallization [24, 25].A smaller initial grain size also reduces the recrystallized grain size due to the increase of potential nucleation sites caused by the increased grain boundary area [24, 25].The recrystallized grain size is also dependent on the temperature. At lower temperatures, finer recrystallized grains are obtained due to the lower mobility of the grain boundaries and consequently a slower growth rate of the recrystallizing grains occurs [25]. The slower growth rate promotes additional nucleation during recrystallization which consequently gives smaller recrystallized grains [20].Recrystallization during deformation is called dynamic recrystallization. If dynamic recrystallization occurs, the flow-stress raises to a peak value followed by a lower steady-state flow-stress [20]. Dynamic recrystallization is promoted by low strain rates and high temperatures. If the strain rate is low enough and the temperature high enough the flow stress does not reach a steady-state flow-stress after the peak, but oscillates around a certain value due to successive cycles of recrystallization occurring concurrently with the deformation [26].

At higher strain rates there is a single peak behavior of dynamic recrystallization. According to Sakai and Jonas [27], the single peak in the flow-stress curve obtained when the strain rate is increased and the temperature is decreased, it involves grain refinement. Decreasing the strain rate and increasing the temperature gives multiple peaks in the flow-stress curve and grain coarsening takes place.

If dynamic recrystallization occurs, metadynamic recrystallization occurs after deformation. If dynamic recrystallization does not occur, static recrystallization may follow the deformation. Static recrystallization requires an incubation time, when the nuclei forms, while the nuclei for metadynamic recrystallization is already present at the end of the deformation [26].

Dynamic recrystallization occurs when a critical strain is reached. The critical strain ε_c, required to initiate dynamic recrystallization is lower than the peak strain, ε_p, in the stress-strain curve [24]. Hence, dynamic recrystallization takes place before reaching the maximum flow stress at the peak strain. According to Sellars [24] the relation between the peak strain and critical

strain is $\varepsilon_c = 0.8 \cdot \varepsilon_p$. For strains below the critical strain there is a significant strain dependence on the recrystallization kinetics after deformation, and above there is not strain dependence.

The critical stress and strain (σ_c and ε_c) for the onset of dynamic recrystallization can be determined by tracking the variations of the strain hardening rate ($\vartheta = d\sigma/d\varepsilon$) of a material during hot deformation [28].

Also, the plastic work done per unit volume of sample until the critical strain and peak strains (W_c and W_p, respectively) was calculated using the following equation [29].

$$W = \frac{1}{\rho} \int_0^z \sigma \, dz \qquad (15)$$

At strains lower than ε_c, work hardening due to the generation of dislocations and dynamic recovery are dominant. At ε_c, dynamic recrystallization is triggered. With the increase of strain from ε_c, the dynamic recrystallized fraction increases gradually and the softening rate increases as a consequence of nucleation and growth of new dislocation free grains. Finally, the initiation of steady state deformation coincides with completion of first dynamic recrystallization cycle. Therefore, the steady state strain (ε_{ss}) can be considered as the strain at which dynamic recrystallization becomes complete [30].

2.4.3.1. Classical nucleation

One of the first recognized theories for nucleation of recrystallized grains is that of Burke and Turnbull [31]. Their theory is based on random thermal fluctuations of the atoms which lead to the formation of strain-free regions or small "crystallites", surrounded by high angle grain boundaries. Such crystallites would only be stable if the energy of their boundaries were lower than the differences in energy between a given crystallite and the deformed matrix. Such a nucleus would have an orientation close to that of the matrix. This mechanism, although it accounts for the incubation period before the onset of recrystallization, has been dismissed as a viable nucleation mechanism [19].
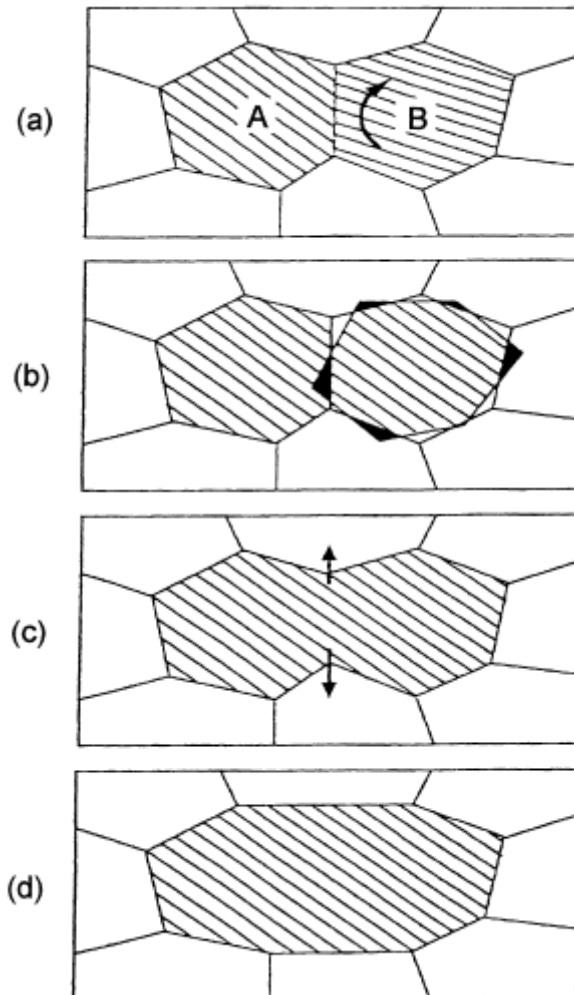
2.4.3.2. Subgrain growth

A material may form a cell structure or subgrains either during deformation or in subsequent recovery. These subgrains are usually areas of approximately dislocation-free material surrounded by low angle grain boundaries. It is possible that such boundaries, by a process of climb and rearrangement, are able to move through the material. As they move through the material they will "sweep up" dislocations either from the matrix or other boundaries. At the same time the size of the subgrain will increase and eventually the size advantage will be reached and the subgrain will form a nucleus. The boundaries of such nuclei will move through the material and consume the dislocation structure which will give a sharp rise in the release of the stored energy and so the rate of growth will increase rapidly [32].

2.4.3.3. Subgrain coalescence

This mechanism was first suggested by Hu [33] and involves, by re-orientation or rotation, a subgrain achieving the same orientation as one of its neighbouring subgrains. The low angle boundary separating the two subgrains then disappears and so a larger subgrain size is achieved. This increase in subgrain size is achieved without subgrain boundary migration. A schematic representation is shown in Fig.4. For the two subgrains to achieve the same

13

orientation one of them must rotate, for example subgrain B can rotate in the clockwise
direction. The dislocations in the disappearing boundary separating the two grains must move,
by climb, from the boundary and material must diffuse from the darkly shaded areas to the
light ones. Once the boundary has disappeared the remaining boundaries on either side of the
cell are in an unfavorable configuration and move outward, so that finally the larger subgrain is
formed [32].

Fig.4. A schematic diagram showing the sub-grain coalescence mechanism for sub-grain growth [34].

The thermodynamics of such a mechanism were studied by Li [35] who showed it to be
energetically favourable. The rate of subgrain coalescence was, however, found to be low and
certainly considerably lower than the rate of subgrain growth.

2.4.3.4. Nucleation at grain boundaries.

The main mechanism for the formation of nuclei at grain boundaries is by the bulging of part
of the boundary, due to differences in dislocation density on either side, which produces a
strain-free region. The mechanism was first observed by Beck and Sperry [36] and is referred
to as strain-induced grain boundary migration (SIBM). The orientations of the new grains
formed are expected to be similar to that of the one of the parent grains and so this

mechanism will leave a retained rolling "R" texture after recrystallization. The mechanism is shown schematically in Fig. 5
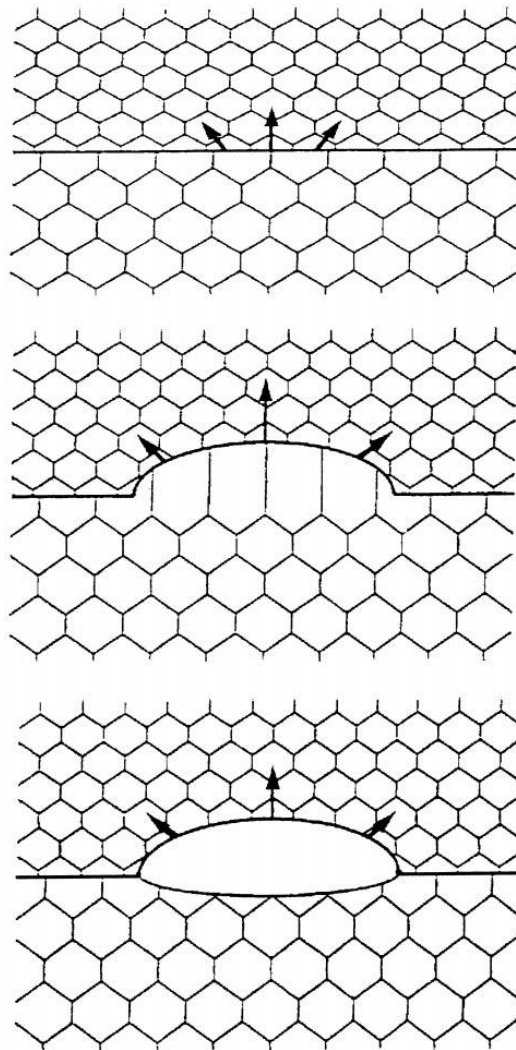
Fig.5. A schematic diagram showing strain induced grain boundary migration: (a) the difference in dislocation density causes the boundary to bulge upwards, (b) dragging the sub structure of the grain behind the advancing boundary, until (c) the boundary becomes free of the substructure and is allowed to move unhindered through the matrix [19].

The top grain contains a higher dislocation density and so the grain boundary bulges into the grain, dragging the dislocation structure of the lower grain behind it. Eventually these dislocations will anneal out and a strain-free region will be formed. The mechanism is possible as long as the reduction in energy associated with stored energy is higher than the energy increase associated with extending the high angle boundary [32].

The boundary has already a sufficiently high misorientation for it to be mobile, the only other factor that is needed for SIBM is a difference in strain energy between grains in the vicinity of the boundary [19]. This has been explained in a number of ways but is still unclear [32].

15

2.4.3.5.   Nucleation at transition bands

Transition bands are heterogeneities, which have a sharp orientation gradient across them. Dillamore and Katoh [37] developed a model, which predicted that the central region of some transition bands would contain cube-oriented material. Transition bands have generally been observed as bands in the rolling plane of metal, their center regions have the cube orientation, (001), [100]. It is widely accepted that nucleation can occur at these bands by the growth of the cube region [38, 39 and 40] producing, on recrystallization, the cube texture.

2.4.3.6.   Nucleation from shear bands

Shear bands are completely different from transition bands as their formation is dependent on extrinsic factors such as temperature and strain rate [41]. Their effect on the nucleation and consequently in the texture after recrystallization is dependent on the material.
It has been shown that shear bands contain high angle boundaries, able to migrate and so create nuclei [42]. Koken and Embury [42] also showed that nucleation at shear bands, was temperature-dependent, with such nucleation decreasing with increasing temperature. When the temperature is higher they demonstrate that nucleation at grain boundaries became more fertile.

2.4.3.7.   Nucleation at second-phase particles

Many metals contain second-phase particles, of which many are present during deformation. They do not, as a rule, deform significantly during deformation and consequently deformation. The most important particles are usually >1 mm in diameter [43] and the zones formed around them operate as nucleation sites.

Ørsund and Nes [44] studied the effect of large particles in aluminum-manganese alloys and produced a model for the orientations seen in terms of the part of the deformation zone in which the nucleus forms. They found that at low temperatures, the nucleation started in the outer region of the deformation zone, which led to orientations similar to that of the matrix.

At higher temperatures the nucleation started nearer to the particles which appeared to lead to randomly oriented nuclei. In their later paper, they also reported that the transition temperature between nucleation at the core of the zone and the extremities was dependent on the particle size, with a lower transition temperature in alloys containing larger particles [45]. The effect on the recrystallization texture is then dependent on the annealing temperature [32]. Juul Jensen et al. showed similar results in commercially pure aluminum containing large second-phase particles [46]. They showed, however, that the random textures produced by nucleation near the particles were not prolific enough to affect the recrystallization texture, as other types of nuclei dominated. Hansen and Bay [47] showed that the presence of large particles also affects the nucleation at other heterogeneities in the deformation structure such as grain boundaries and transition bands.

2.4.3.8.   The effect of small second-phase particles on recrystallization

Large second-phase particles present during deformation act as nucleation sites during recrystallization. If smaller particles are present in the material during deformation then the matrix can, in general, deform around them without the formation of deformation zones of the type required for nucleation sites. It has been shown, however, that they tend to inhibit the nucleation process by pinning the recrystallizing grain boundaries. This effect is not entirely

due to the size of the particles; their spacing is also critical and particles with close spacings, regardless of size, also retard the nucleation of new grains. For a nucleus to grow it must achieve a stable size of approximately 5 mm in rolled Al [48]. If a nucleus cannot attain this size advantage before its boundary becomes pinned by the particles then it will not form a viable nucleus.

2.4.3.9.   *Oriented growth*

Oriented nucleation theories of recrystallization textures are well established, but there has been considerable work on the effect of oriented growth on the development of preferred orientation during recrystallization. The mobility of a boundary is dependent on its misorientation. The effect that oriented growth has on the recrystallization texture has been the subject of some dispute. The main problem with the oriented growth theories and their effect on the texture comes from the non-homogeneous nature of the deformation structure [32]. During deformation a grain may split into many regions which deform with different slip systems. This difference in the deformation will lead to differences in orientation between these regions, with differences of up to 208 being measured over small distances [40]. The significance of oriented growth may be more significant in the development of texture when it occurs in conjunction with oriented nucleation [48].

2.4.3.10.   *Annealing twins*

One important feature of recrystallized microstructures in some materials, which may be directly related to oriented growth, is the formation of annealing twins. Annealing twins are a common microstructural feature of most fcc metals and alloys with low stacking fault energies. They appear in the microstructure as straight boundaries which have misorientations relating to high matching of the lattices on either side of the boundary [49]. Three mechanisms have been suggested for the formation of annealing twins, all of which involve a switch to a twin orientation during recrystallization and grain growth to reduce the interfacial energy between a grain and the matrix into which it is growing. The first was proposed by Dash and Brown [50] who used TEM observations of a Ni±22 %Fe alloy and showed that the annihilation of dislocations near advancing grain boundaries caused the formation of high densities of stacking faults. Annealing twins then nucleated at the grain boundaries and grew into the grains adopting morphology with interfaces parallel to the habit plane of the faults. This morphology is shown schematically in Fig. 6 (a). The switch to a twin orientation may also occur at an advancing boundary if the boundary grows into a region where the orientation between the grain and the matrix is unfavorable for growth [51 and 52]. There will then be an incentive for a switch to the twin orientation to allow further growth of the grain, as shown in Fig. 6 (b). Data obtained from Copper [53] and lead [54], also by Aust and Rutter [55-57]) has been used to suggest that the switch to the twin orientation occurs at triple points as they migrate during annealing. This is shown schematically in Fig. 6 (c) where the twin of grain A nucleates at the triple point between A and B and grows into B. This will be favorable as the energy of the boundary between grain A and its twin is lower than that of the boundary between A and C even with the increase in the total boundary area in the material. The twin will, therefore, be stable and able to grow as the triple point migrates.
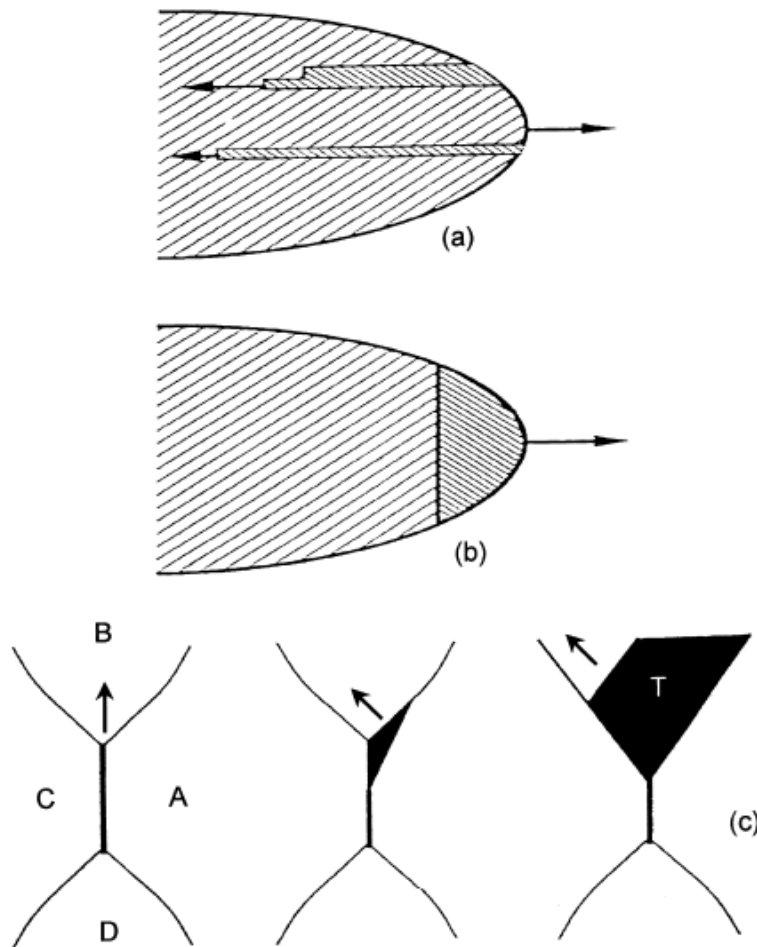
Fig.6. The mechanism for the formation of annealing twins during recrystallization and grain growth: (a) nucleating from an advancing grain boundary due to the annihilation of dislocations near the boundary, (b) by a switch to the twin orientation to lower the energy of the advancing boundary, and (c) forming at a triple point as it moves through the material [59**].**

2.4.4. THE EFFECT OF MICROALLOYING ELEMENTS ON RECOVERY AND RECRYSTALLIZATION IN STEELS

Microalloying elements retard the progress of recrystallization in steels either as dissolved in the austenite (solute drag) or as precipitates (precipitation pinning). The most common microalloying elements are niobium, vanadium and titanium which are all strong carbide-forming elements [20].

The softening behavior in V steel is not influenced by an increase of C or N. Recrystallization is most likely complete before the start of VC or VN precipitation. The reason for the small effect of V on softening was determined to be the weak solute drag effect that does not retard the recovery and the onset of recrystallization [20].

Precipitation and recrystallization are two interacting processes. If precipitation occurs before or in the initial stage of recrystallization, recrystallization is retarded by the precipitates. If

recrystallization is complete before the onset of precipitation, precipitation kinetics is reduced due to fewer nucleation sites [20].

Finally, precipitates are considered as potential sites for the nucleation of intergranular cavities. The dynamic recrystallization delay or the grain boundary migration slowing down due to the above mentioned precipitates, favor the nucleation of cavities during intergranular sliding [58].

2.4.4.1.   Microstructure evolution during hot working

During deformation three main microstructural changes occur. The first is the change in the shape of the grains that exist in the pre-worked material. During rolling the grains become elongated in the direction of rolling. The second feature is the formation of structures within the grains, which are associated with the buildup of dislocations. The third change is the formation of macroscopic features, which are usually referred to as deformation bands; transition bands, kink bands and shear bands.

Another important feature is the formation of preferential orientations or texture because of the rotation of the crystal lattice relative to the overall material. This texture becomes stronger as the amount of deformation increases and will ultimately affect the texture development during the recrystallization process. A structure is developing within the grains during the deformation due to the buildup of dislocations. The first structures consist of dislocation tangles and, as the strain increases, these tend to become ordered into two-dimensional dislocation walls, which surround regions with a lower dislocation density. When the strain is higher, the grains begin to separate into individual three-dimensional regions, which are referred to as cell structures or "blocks". The boundaries between these cells have a higher dislocation density than those of the subgrains and usually the misorientation across the boundary is high. These cell blocks are, in turn sub-divided into cell structures of dislocation tangles and, as the strain increases, the size of both the cell blocks and the interior cells decrease [58].

2.5. FLOW INSTABILITY PROCESSES

2.5.1. FLOW LOCALIZATION

The phenomenological criterion of Semiatin and Lahott (1981) and Semiatin and Jonas (1984) for flow localization is given by [59]:

$$\alpha = \frac{1}{\dot{\varepsilon}} \frac{d\dot{\varepsilon}}{d\varepsilon} = -\frac{\gamma}{\sigma\,m} \qquad (16)$$

Where $\dot{\varepsilon}$ is the strain rate, ε is the strain, γ is the work hardening rate, m is the strain rate sensitivity and σ is the flow stress (positive), This has been applied to identify regions of flow localization. The regimes where α >5 are concluded as the regimes of flow localization in titanium alloys [59].

2.6. PHASE TRANSFORMATION

Ferrite, cementite and pearlite are the major constituents of the microstructure of plain carbon steels as they are subjected to relatively slow cooling rates while martensite and/or bainite appears at higher cooling rates.

Rapid quenching of austenite to room temperature often results in the formation of martensite, a very hard structure in which the carbon, formerly in solid solution in the austenite, remains in solution in the new phase.

The martensitic reaction it is usually obtained at a rate of cooling sufficiently high to suppress the higher temperature diffusion-controlled ferrite and pearlite reactions, as well as other intermediate reactions such as the formation of bainite.

Bainite also occurs during continuous cooling at rates too fast for ferrite and pearlite to form, yet not rapid enough to produce martensite [60].

3. EXPERIMENTAL

3.1. MATERIAL

One type of microalloyed steel was used and its lot number is "314". The size of the samples was 10 mm of length and 5 mm of diameter.

The composition in weight percent of the samples is:

Table 1: Content in wt% of the alloy

314	C	Mn	V	N	Ti	Si	Nb	Al	Cr	Ni	Cu
Wt%	0.165	1.470	0.099	0.006	0.002	0.017	0.002	0.019	0.033	0.019	0.026

In the following table the size of the dilatometry samples (L = length and ϕ = diameter) is shown. Samples are cut plane-parallel.

Table 2: Size of the samples:

1		2		3		4		5		6	
L (mm)	ϕ (mm)	L (mm)	ϕ (mm)	L (mm)	ϕ (mm)	L (mm)	ϕ (mm)	L (mm)	ϕ (mm)	L (mm)	ϕ (mm)
9.93	4.94	10	5.1	9.88	4.99	9.96	4.99	9.97	5.1	9.99	4.95

3.2.DILATOMETRY

Dilatometry experiments have been done in a Dilatometer Type 805 AID FROM THE Bähr company.

Before starting the experiments a thermocouple of type S was welded in the middle of the sample to control the temperature.

Three different heat treatments cooled down with helium or slowly were carried out and can be seen in Figure 7.
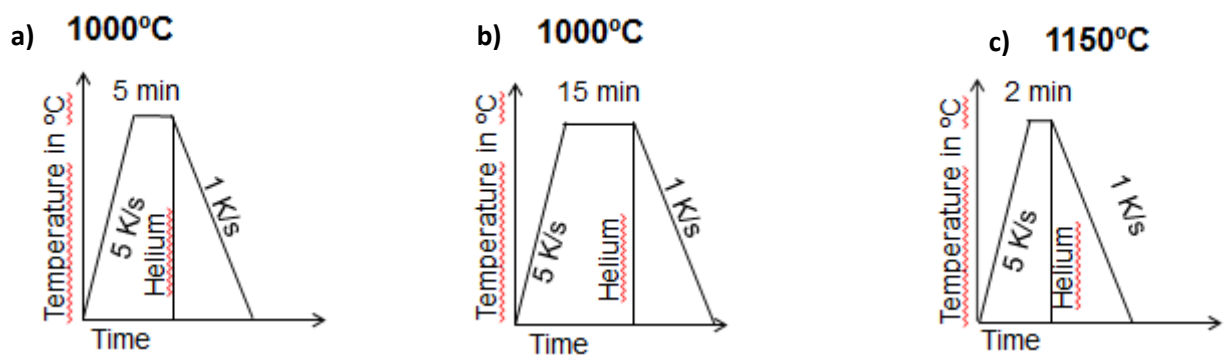
Fig.7. Shows the different heat treatments carried out in the dilatometer.
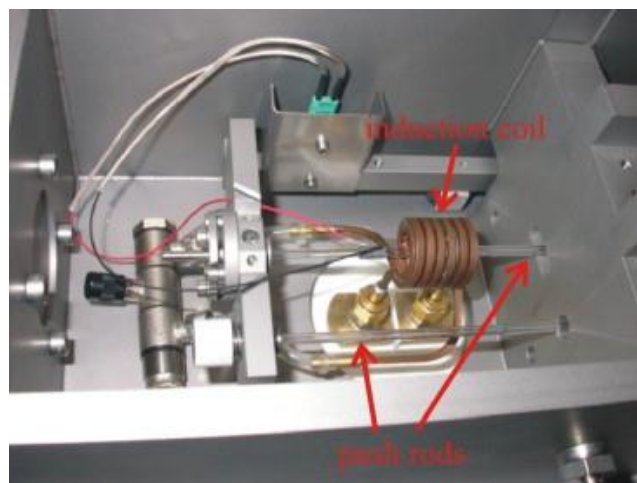
In Figure 8 the dilatometer is shown and its main parts are indicated with arrows.

Fig.8. Shows the dilatometry and its different parts.

3.3.METALOGRAPHY

Metallography is done to get information about the microstructure of the material such as size and form of grains, grains boundaries and phases.

The region of the sample must be selected in the area that it needs to be studied and in the right orientation. Thus, samples are cut with metal saws with abrasive blades and refrigerated with water or special fluids. The studied material should not be overheated because the microstructure can be modified with high temperatures. Afterwards the sample must be embedded with a chemically inert material respect the material of the sample.

The grain and the features of the steel can only be seen if grinding and polishing are carried out.

Dilatometry as well as hot deformed samples were cut in longitudinal direction embedded with Duro Fast and ground with SiC paper up to 4000. Then the samples were polished with lubricant blue and diamond paste of 1μm. The grinding was done with water and the polishing with alcohol.

The objective of the etching is to make visible the structural features of the metal or alloy. This is achieved through a proper reagent that undergoes the polished surface to a chemical reaction. The reagent can consist in organic or inorganic acids and alkalis dissolve in alcohol, water or other solutes. The following table shows the reagents for steels used in this work.

Table3: Reagents of etching [10 and 61]

METAL	REAGENT	COMPOSITION	OBSERVATION
Iron and carbon steel	Nital	2 to 5% nitric acid in methyl alcohol	Obscure the pearlite in carbon steel. It differentiates the pearlite from the martensite. It shows grain boundaries Time: from 5 to 60 seconds.
	Beraha I	100 ml water, 0.6ml HCl and 1g $K_2S_2O_5$	Ferrite is white, martensite is black or dark brown or blue and the bainite and tempered martensite is light brown .

The samples are immersed into the solution to etch them. The etching time must be controlled very carefully. If the etching time is too short, grain boundaries and other features will be blurred and vague when they are observed in the microscope. If the etching time is too long, the sample will be over etched and the microstructure will be very dark, showing unusual colors.

After etching the sample is put under a water jet and afterwards cleaned with alcohol. In this work the samples were etched either with Nital or Beraha I for comparison. The microstructure was observed in a Light Optical Microscope (LOM) at different magnifications. The microscope was the Observer Z1m from the brand Zeiss.

The Figure 9 shows the Light Optical Microscopy with which the pictures were taken.


Fig 9. Light optical microscopy

3.4. GLEEBLE

The compression tests were carried out in a Gleeble® 3800 machine. The tested samples were about 15 mm of length and 10 mm of diameter.
Two pairs of thermocouples (type K) were weld at the middle and at two millimeter from the edge of the sample. Foils of molybdenum and graphite were put between the sample and the anvil to reduce the gradient of temperature and to reduce the friction, avoiding that the sample sticks on the anvil. The used atmosphere in the chamber of the Gleeble was argon.
 The Gleeble® 3800 machine use a servohydraulic system to hold the sample and then compress it. The Gleeble® 3800 machine uses an electric current to heat up the samples and the strain and strain rate is introduced before the start of the experiment. Thereby the change in length is controlled to be 7mm.
For comparison, heat treatments were carried out without deformation at samples. The samples were heated with a rate of 5 K/s to 1000°C or 1150°C and hold for 2, 5 or 15 minutes.
In Figure 10 a schema of the Gleeble and the main components to carry out the heat and deformation treatments is shown.
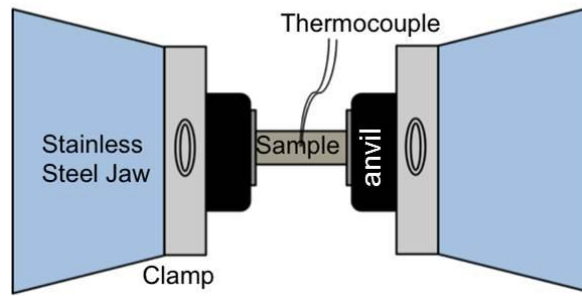
Fig.10. Schematic representation of the Gleeble.

The Figure 11 shows a photograph of the Gleeble® 3800 in which the heat treatments as well as compression tests were carried out.

Fig.11. Closed chamber of the Gleeble® 3800

The different heat treatments were:

A) Heating to 1000°C with 5 K/s, holding for 5 minutes and water quenching.
B) Heating to 1000°C with 5 K/s, holding for 15 minutes and water quenching.
C) Heating to 1150°C with 5 K/s, holding for 2 minutes and water quenching

After observing the microstructures, the compression tests were carried out using austenitization method c) and cooled down with 1 K/s to the deformation temperature. The experiments were carried out at 750-850-959-1050-1150°C and 0.01-0.1-1-10-80/s, making a total of 25 parameters. The strain rate 80/s was the largest achievable.

Figure 12 shows a schematic representation of the deformation tests that were carried out in the Gleeble machine.
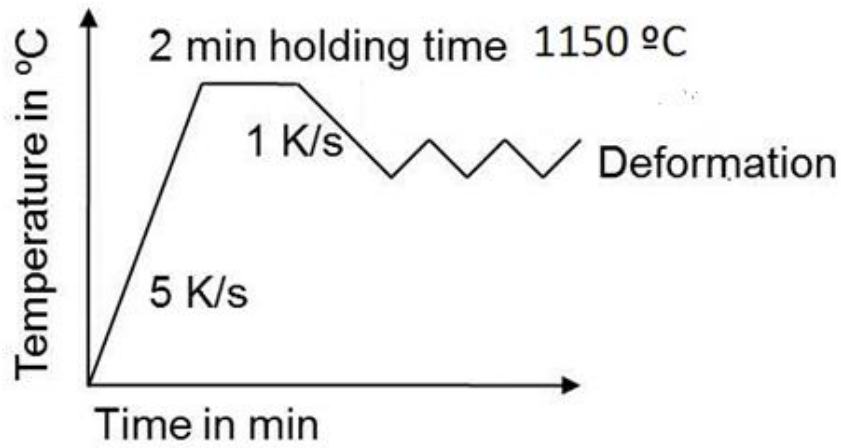
Fig.12.Compression test that were carried out in the Gleeble®3800 machine

4. RESULTS

4.1.   DILATOMETRY

The graphics shown in Figure 13 correspond to each heat treatment was carried out in the dilatometer. Figure 12 represent the change in length with the temperature.

The critical temperatures Ac_1, Ac_2, Ac_3, Ar_1, Ar_3, Bs, Ms and Mf, which are the points of the critical temperatures in which a phase transformation occurs, can be obtained. They were obtained using the tangent method. This can be seen in Figure 13.

a)

b)
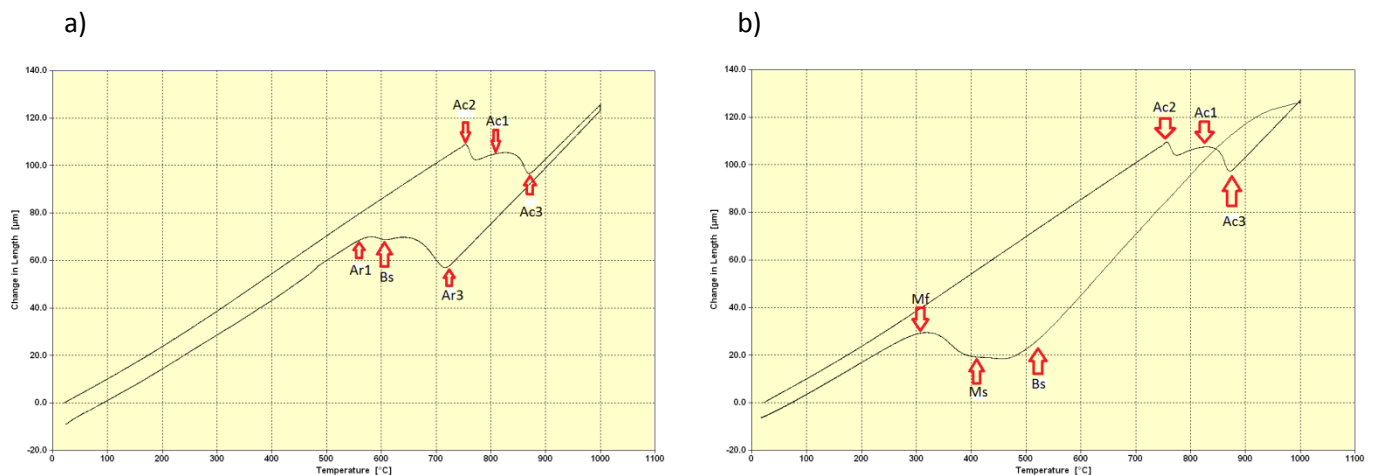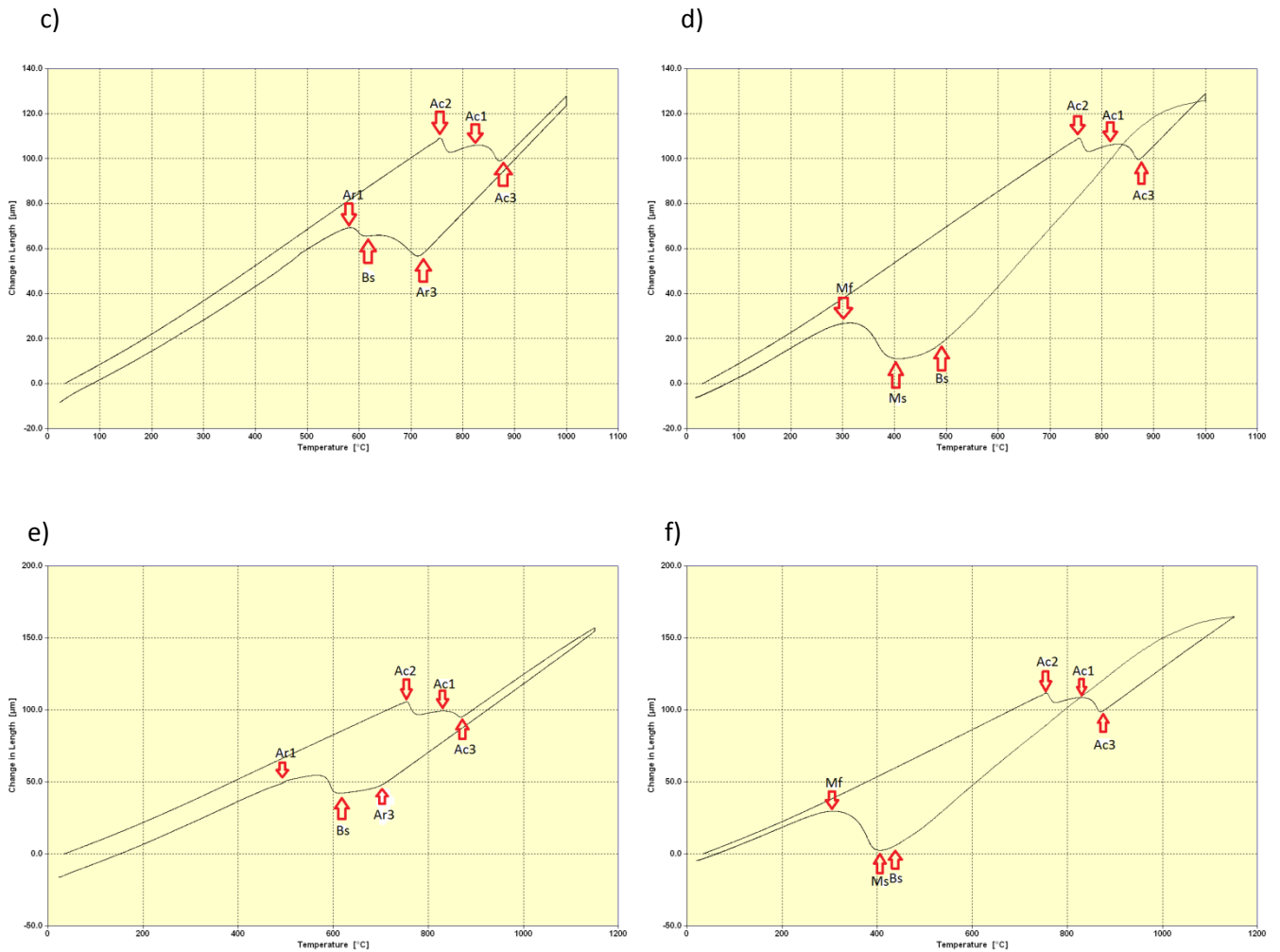
Fig.13. Phase transformation temperatures in dilatometric curves of low alloyed steel 314, (a) Heating to 1000ºC with 5K/s, holding for 5 min and cooling with 1 K/s, (b) Heating to 1000ºC with 5K/s, holding for 5 min and cooling with Helium, (c) Heating to 1000ºC with 5K/s, holding for 15 min and cooling with 1 K/s, (d) Heating to 1000ºC with 5K/s, holding for 15 min and cooling with Helium,(e) Heating to 1150ºC with 5K/s, holding for 2 min and cooling with 1 K/s, (f) Heating to 1150ºC with 5K/s, holding for 2 min and cooling with Helium.

The temperatures of the phase transformation are shown in the following table

Table 4: Phase transformation temperatures at different heat treatments

	PHASE TRANSFORMATION TEMPERATURES (ºC)							
NUMBERS	Ac1	Ac2	Ac3	Ar1	Ar3	Bs	Ms	Mf
314-1	813.04	752,57	869.56	565.21	728.26	606	-	-
314-2	808.69	752.17	873.91	-	-	620	407	291.34
314-3	813.04	752.17	878.26	569.56	721.73	613	-	-
314-4	811.11	751.85	874.07	-	-	478	403	285.18

| 314-5 | 816.66 | 752.38 | 876.19 | 552.38 | 723.80 | 610 | - | - |
| 314-6 | 819.04 | 757.14 | 878.57 | - | - | 430 | 405 | 280.95 |

4.2.FLOW BEHAVIOUR

The flow curves of the material at different temperatures and strain rates were obtained with the compression tests carried out in the Gleeble machine. In Figure 13 the flow curves at different temperatures and the same strain rates are shown.
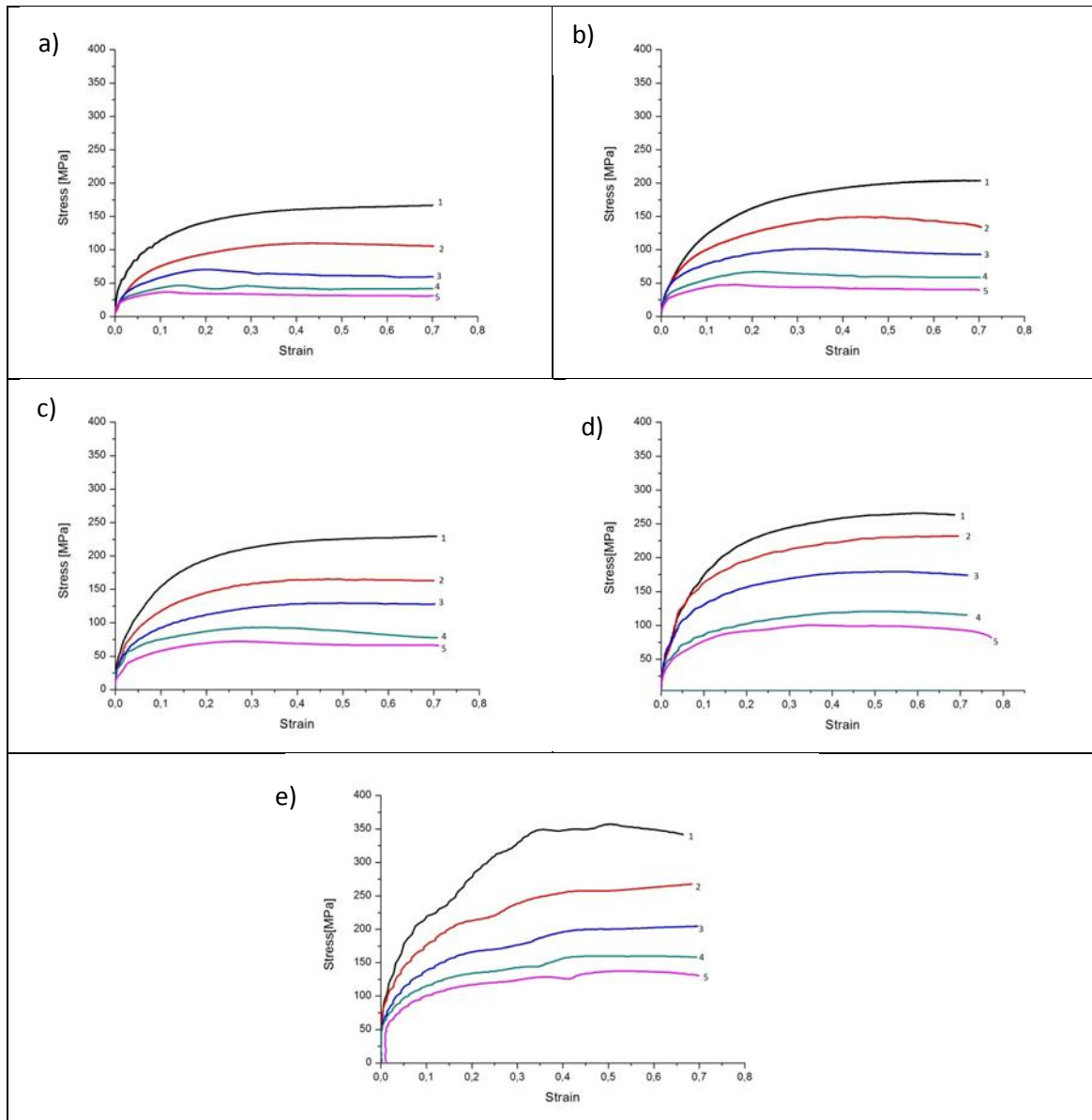
Fig.14. Flow curves at different strain rates: a) 0.01 s^{-1}; b) 0.1 s^{-1}; c) 1 s^{-1}; d) 10 s^{-1}; e) 80 s^{-1}. The temperatures at which the compression after austenitization were carried out: 750ºC (1); 850 ºC (2); 950ºC (3); 1050ºC (4);

4.3.PROCESSING MAPS

Processing maps were calculated using the equations of Murty/Rao [13]. The isolines show the efficiency at different strain rates and temperatures. The dashed area represents the zone of instability calculated with the K_j equation [14].

$$k_j = \frac{\partial lnJ}{\partial ln\varepsilon} - 1 \qquad (17)$$

The m maps were built using equation (3).

4.3.1. PROCESSING MAPS AT A STRAIN OF 0.3

Figure 15 (a) shows the processing maps calculated using strain of 0.3. In this case the area with a higher efficiency is at high temperatures, 1150°C, and a strain rate of 1s^{-1}. The instability area is located at high strain rates and temperatures between 825°C and 1025°C. The Figure 14 (b) shows the m map with similar tendencies than the η map and it does not show any instability area.
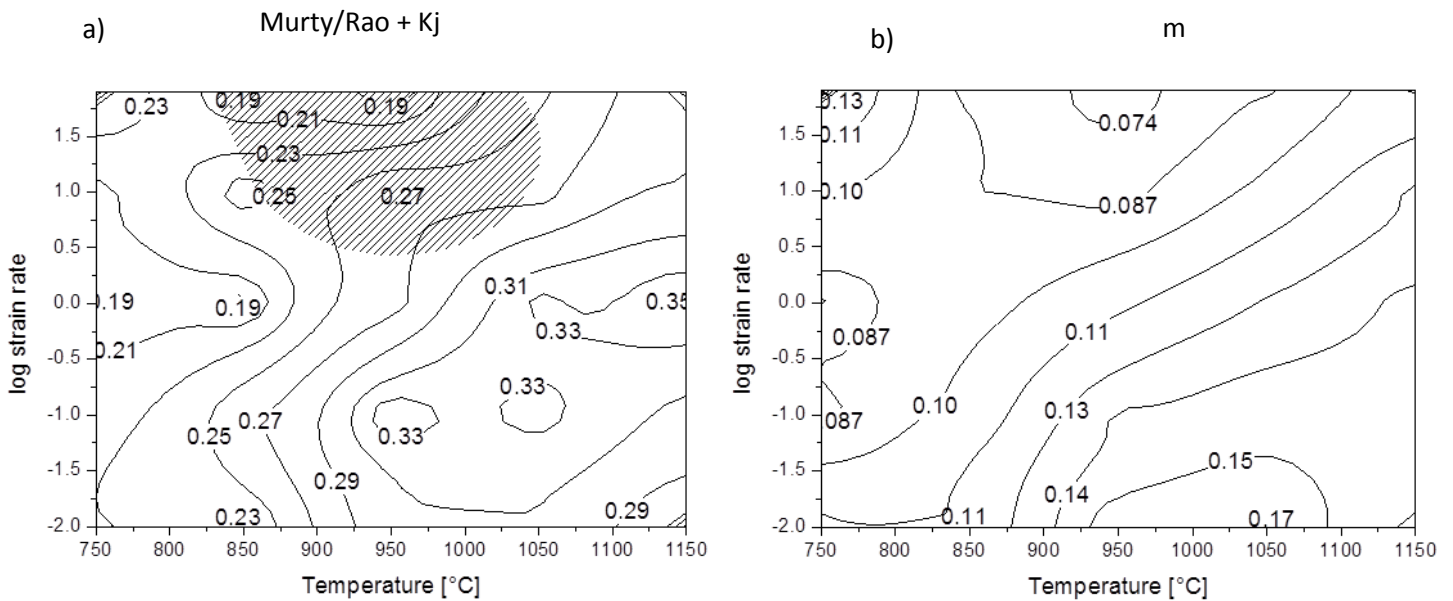
a) Murty/Rao + Kj   b)   m

Fig.15. (a) Processing map of Murty/Rao + K_j and (b) *m* map at strain of 0.3. The isolines represent the efficiency value η and the dashed area, predicts instability.

4.3.2. PROCESSING MAPS AT A STRAIN OF 0.4

In Figure 16 the processing maps are calculated for (a) Murty/Rao and K_j, (b) the m,(c) Murty/Rao and $k_{Murty/Rao}$ and (d) Prasad. In this case when the efficiency is calculated according the Murty/Rao criteria the highest efficiency can be detected again at high temperatures and a strain rate of 1s^{-1}. In general, the efficiency values are comparable, but the instability area

different when it is calculated according to different criteria. In the case of k_j the instability area is located at high strain rates and temperatures between 900°C and 1000°C. For $k_{Murty/Rao}$ the instability area almost covers the whole map. The m map does not predict any instability area. The η_{Prasad} map has an instability area at low-middle temperatures and low-middle strain rates.
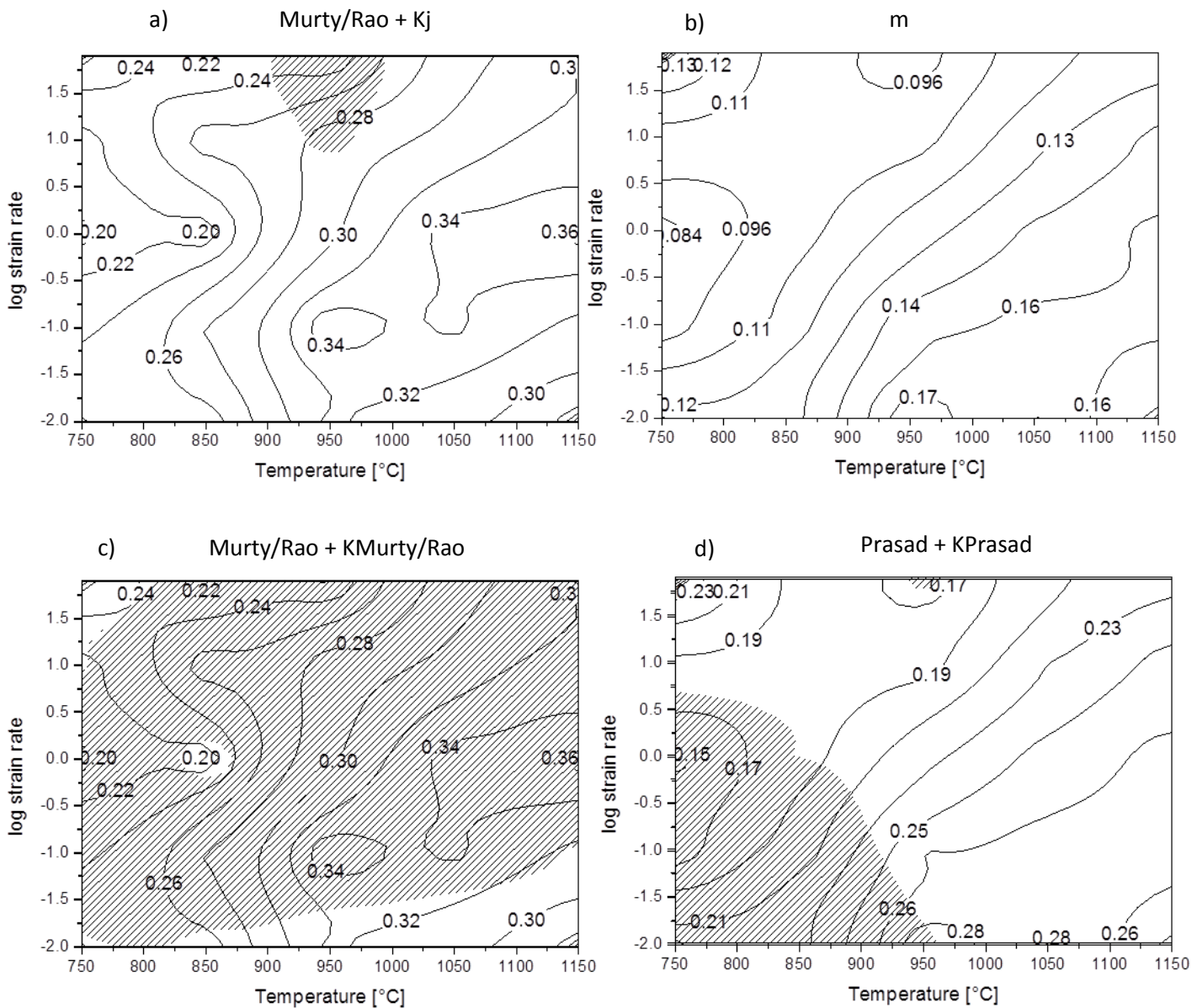
Fig.16. (a)Processing map of Murty/Rao + Kj , (b) m map, (c) Murty and Rao with K of Murty and Rao and (d) processing map of Prasad + K of Prasad, all of them at strain of 0.4. The isolines represent the efficiency value η and the dashed areas predict instability.

4.3.3. PROCESSING MAPS AT A STRAIN OF 0.5

Figure 17 (a) shows the processing map calculated according the *Murty/Rao* and k_j criteria. The highest efficiency is located at high temperatures and middle-high strain rates. The instability appears at high strain rates and temperatures between 800°C and 950°C. The Figure 16 (b) shows the m map similar to the m map at 0.4 of strain.
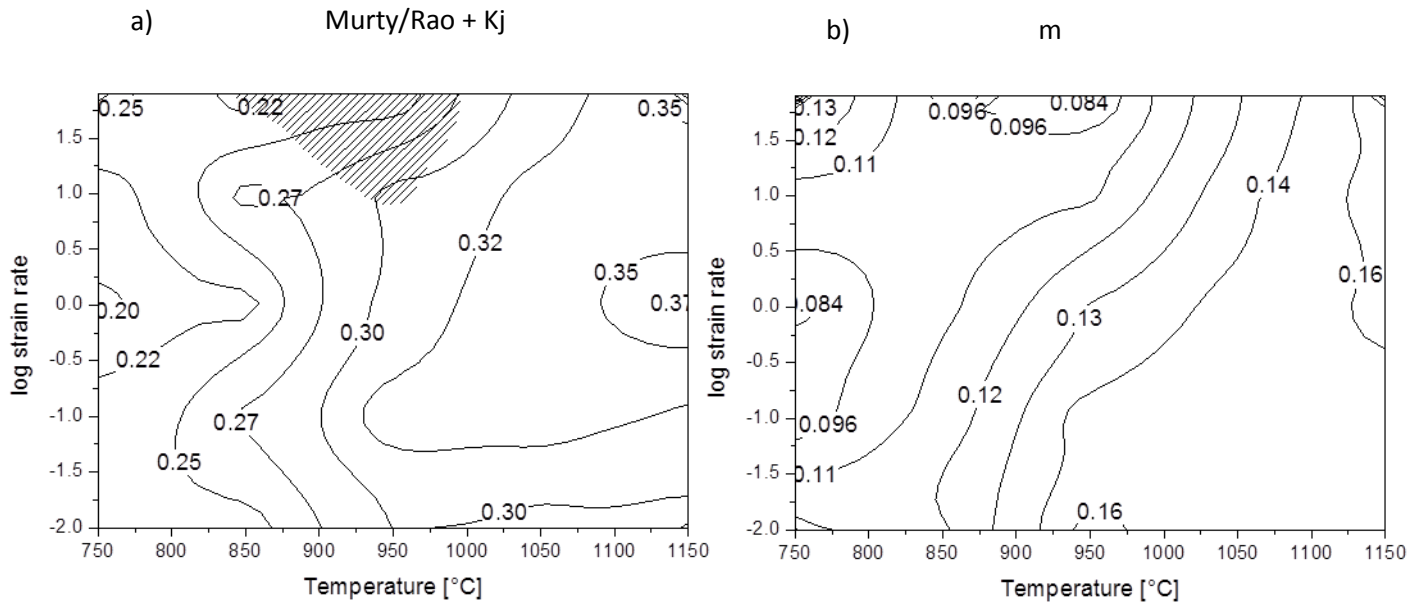
Fig.17. (a)Processing map of Murty/Rao + Kj and (b) m map at strain of 0.5. The isolines represent the efficiency η and the shadow area predicts instability.

4.3.4. PROCESSING MAP AT A STRAIN OF 0.6

Figure 18 shows the processing map calculated according to the *Murty/Rao + k_j* criteria (a) and the m map (b). The higher values of efficiency appear at high temperatures and middle-high strain rates in both cases and in general the tendency of the values is the same. The instability area is located at high strain rates and temperatures between 875°C and 975°C in the first map, while the m map does not show instability.
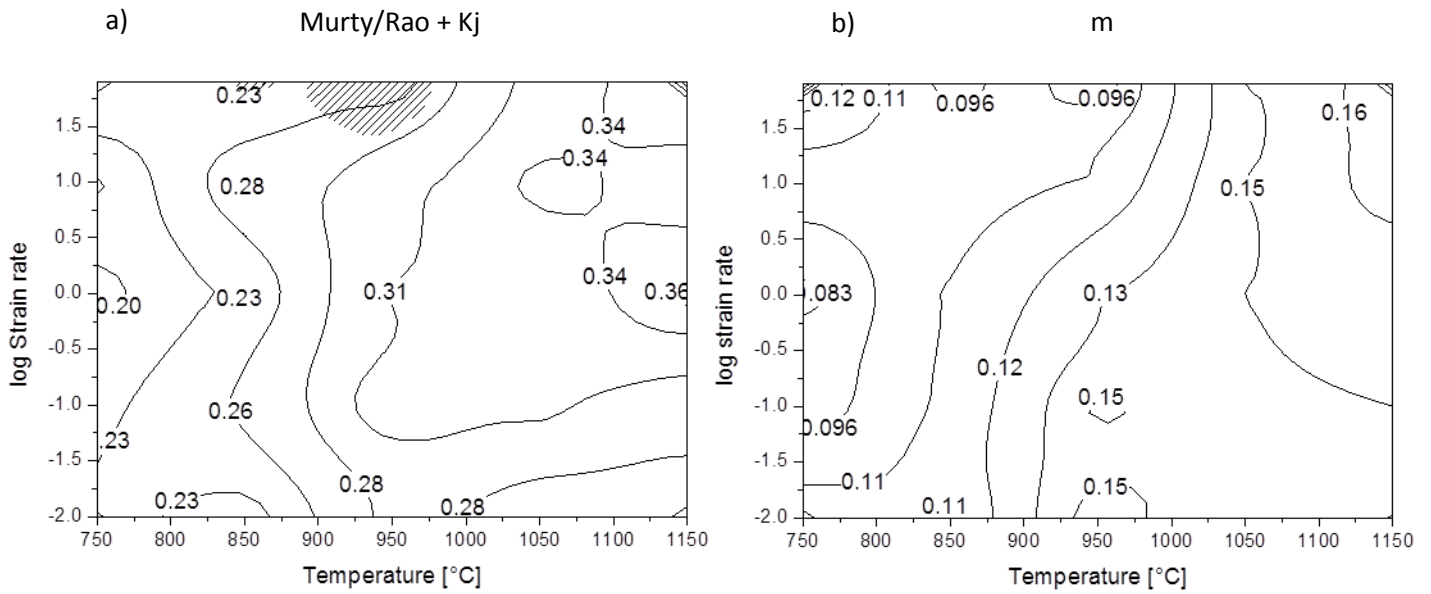
a) Murty/Rao + Kj   b)   m

Fig.18. (a)Processing map of Murty/Rao + Kj and (b) m map at strain of 0.6. The isolines represent the efficiency η and the shadow area predicts instability.

4.4.FORCE

The following table shows the maximum force carried out for the Gleeble® 3800 machine during the compressions test. The Force is measured in kN.

Table 5: Force during compression tests.

Temperature[ºC]/Strain rate [s⁻¹]	0.01	0.1	1	10	80
750	27.5	32.5	37	42	52.5
850	17	22.5	26.5	37	42
950	9.7	16.2	21	28.2	32.5
1050	6.75	9.9	12.9	18.5	25.5
1150	5.6	6.9	10.8	13.2	22.5

4.4.1. DILATOMETRY TESTS

The following pictures show the result of the dilatometer heat treated samples. It can be seen in the Figure 19 (a), (c) and e) the ferrite in white and the perlite in black meanwhile in the

Figure 19 (b), (d) and (f) the dark needles are martensite, some bainite is observed in(b) and (d).
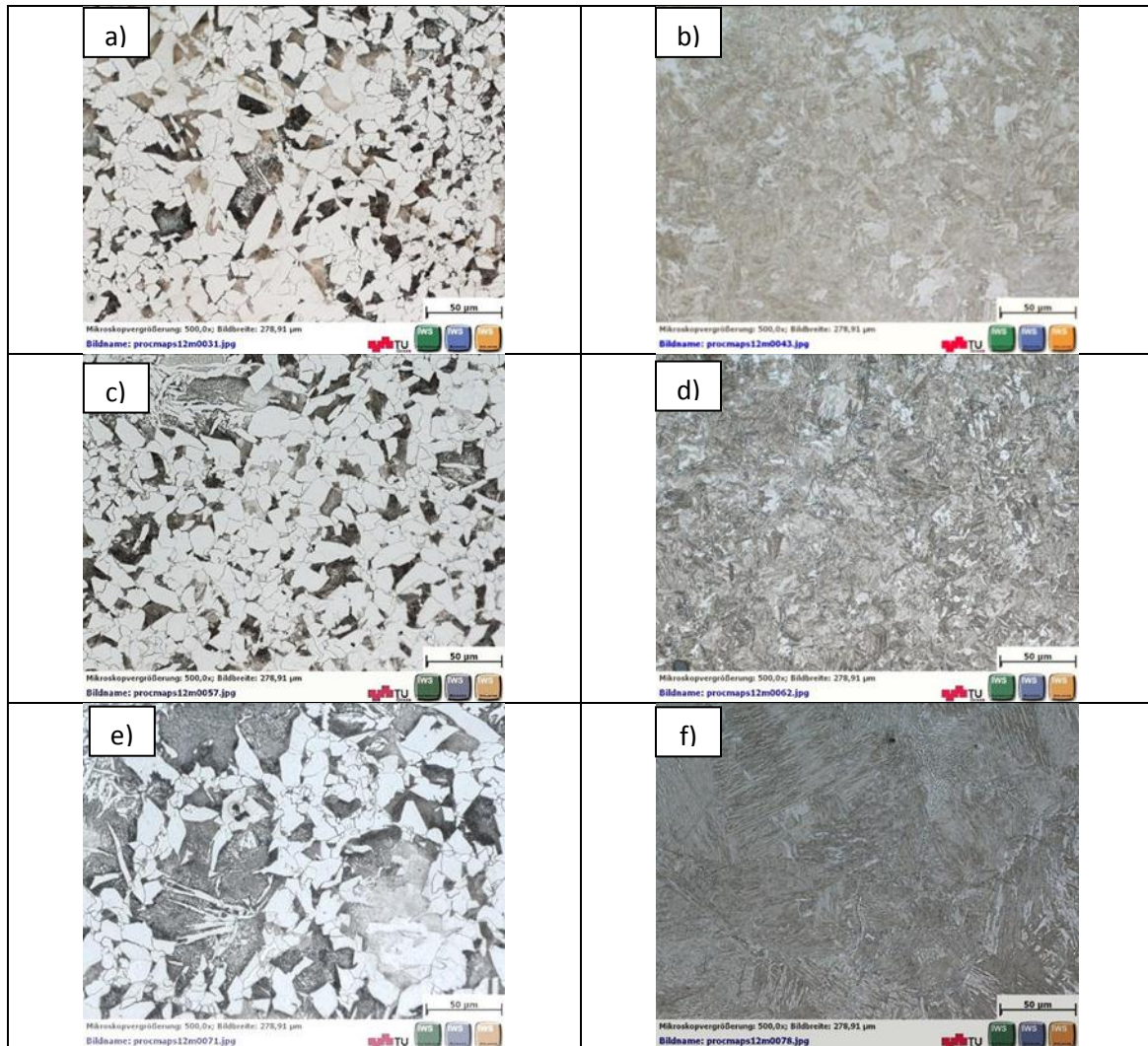
Fig.19. Light optical micrographs showing the microstructure of the material after (a) heating up to 1000ºC with 5 K/s, holding 5 minutes and cooling with 1 K/s, (b) heating up to 1000°C with 5 K/s, holding 5 minutes and cooling with Helium, (c) heating up to 1000°C with 5 K/s, holding 15 minutes and cooling with 1 K/s, (d) heating up to 1000°C with 5 K/s, holding 15 minutes and cooling with Helium, (e) heating up to 1150°C with 5 K/s, holding 2 minutes and cooling with 1 K/s, (f) heating up to 1150°C with 5 K/s, holding 2 minutes and cooling with Helium. All the samples were etched with a solution of Nital 2%.

A second etching method was used to better identify the phases. The samples were etched with Beraha I reagent which showed to be especially useful for the cases in which the samples were cooled very fast. The Figure 20 (b), (d) and (f) shows the ferrite in white, the martensite dark brown or blue and the bainite or tempered martensite in light brown [60].
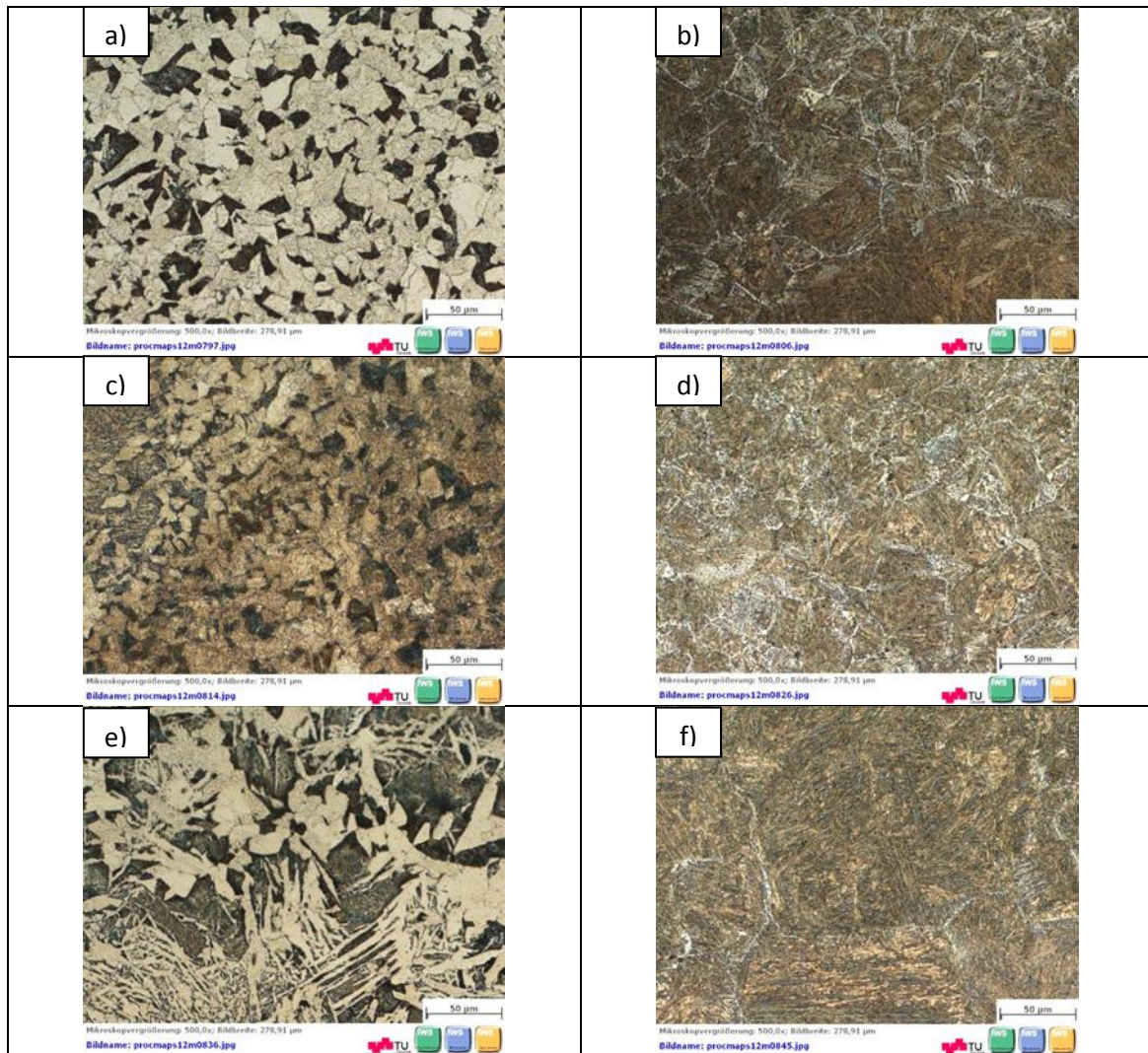
Fig.20. Light optical micrographs showing the microstructure of the material after (a) heating up to 1000°C with 5 K/s, holding 5 minutes and cooling with 1 K/s, (b) heating up to 1000°C with 5 K/s, holding 5 minutes and cooling with Helium, (c) heating up to 1000°C with 5 K/s, holding 15 minutes and cooling with 1 K/s, (d) heating up to 1000°C with 5 K/s, holding 15 minutes and cooling with Helium, (e) heating up to 1150°C with 5 K/s, holding 2 minutes and cooling with 1 K/s, (f) heating up to 1150°C with 5 K/s, holding 2 minutes and cooling with Helium. All the samples were etched with the solution of Beraha I

4.4.2. LIGHT OPTICAL MICROSCOPY AFTER COMPRESSION TESTS.

These pictures were taken after compression tests in situ water quenching. In the Figure 21 the needle of martensite in brown and the equiaxed ferrite grains in white at the prior austenitic grain boundaries can be seen.
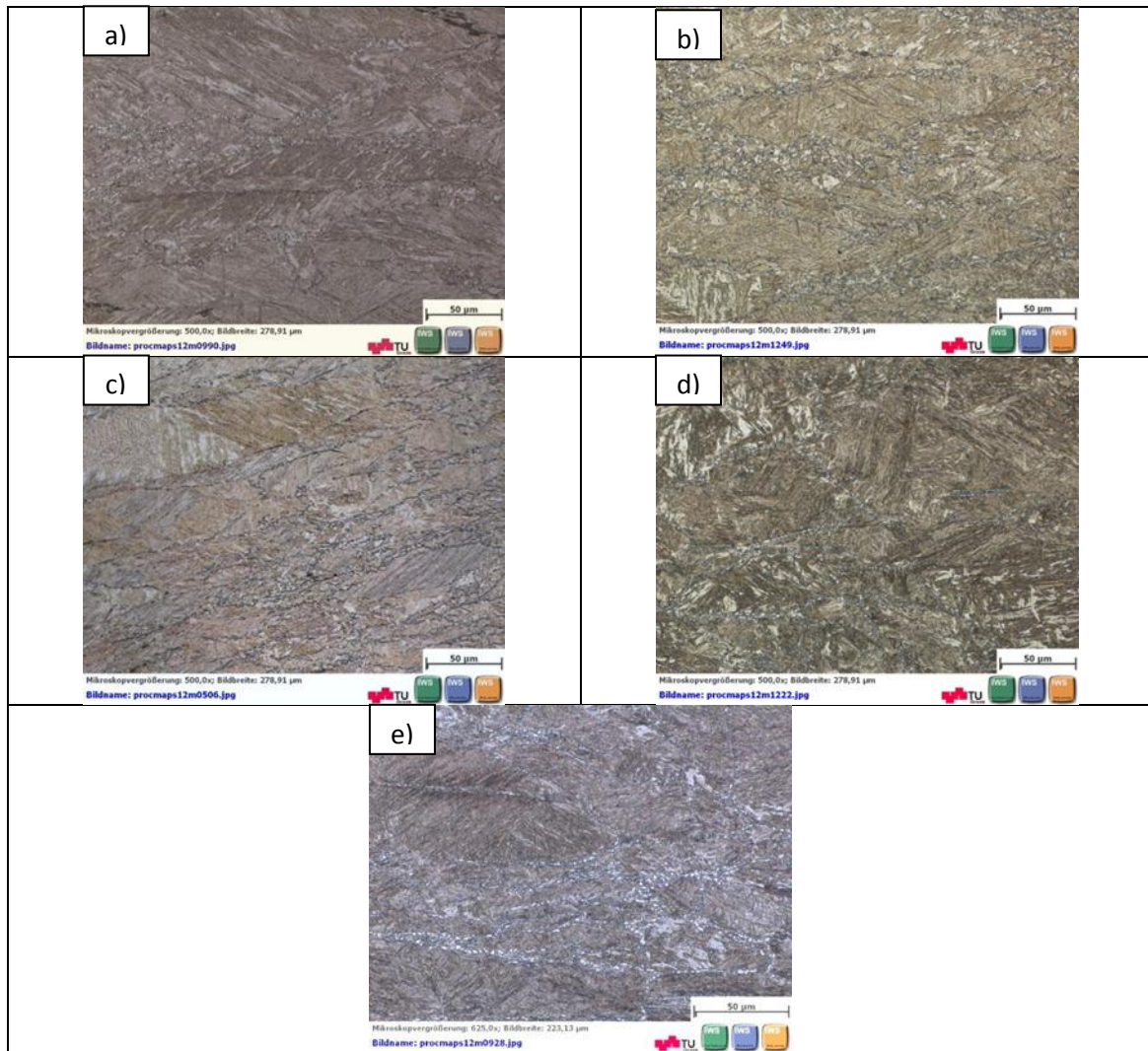
Fig.21. Light optical micrographs showing the microstructure of the material after compression test at 750ºC in the middle (a) strain rate of $0.01s^{-1}$, (b) strain rate of $0.1s^{-1}$, (c) strain rate of $1s^{-1}$, (d) strain rate of $10s^{-1}$, (e) strain rate of $80s^{-1}$. Magnifiaction 500x.

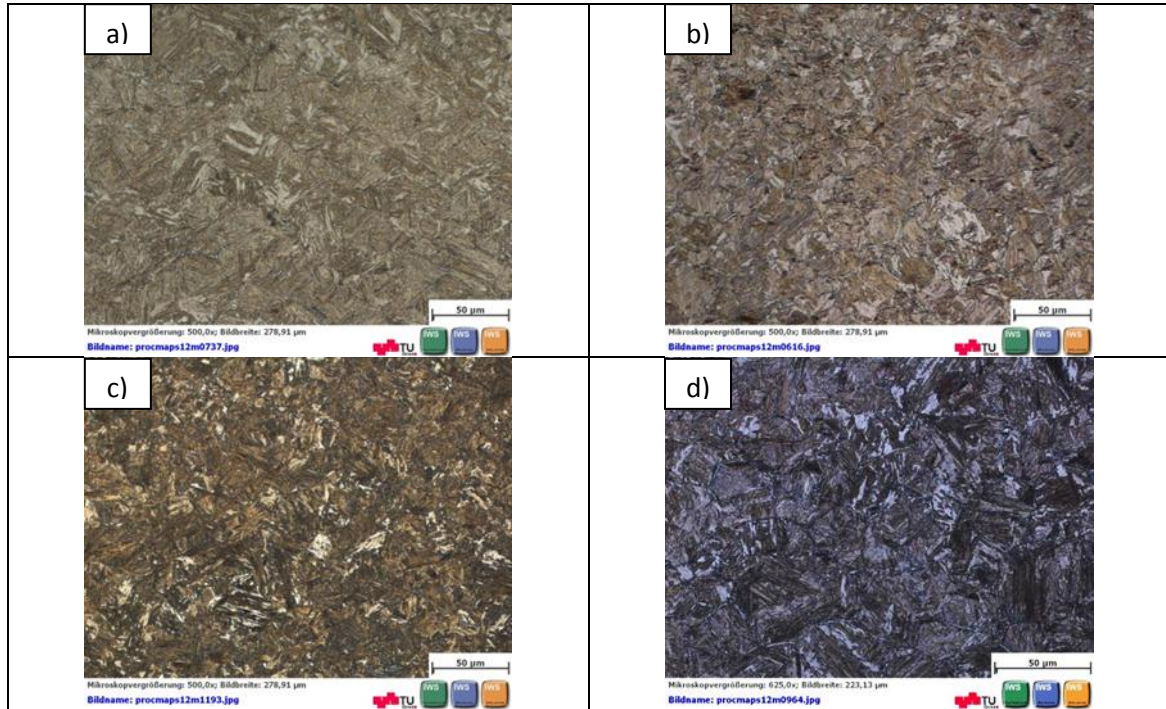In Figure 22 the acicular form of the martensite in dark brown, the bainite in light brown and the white equiaxed ferrite can be seen
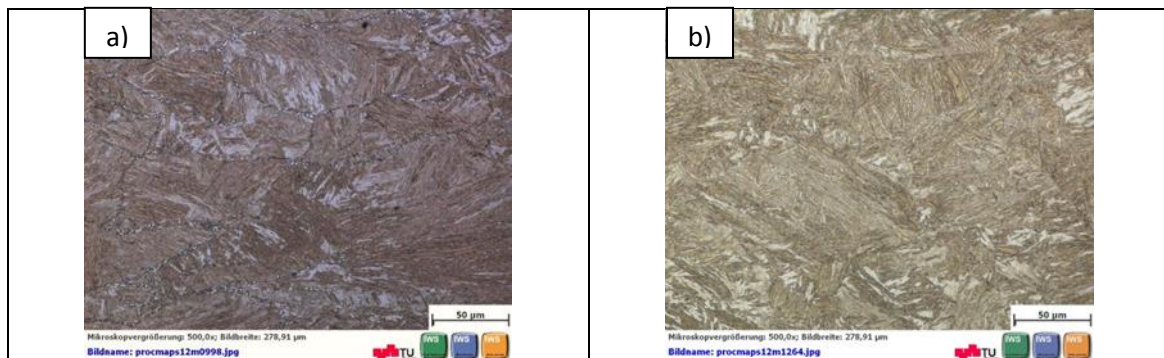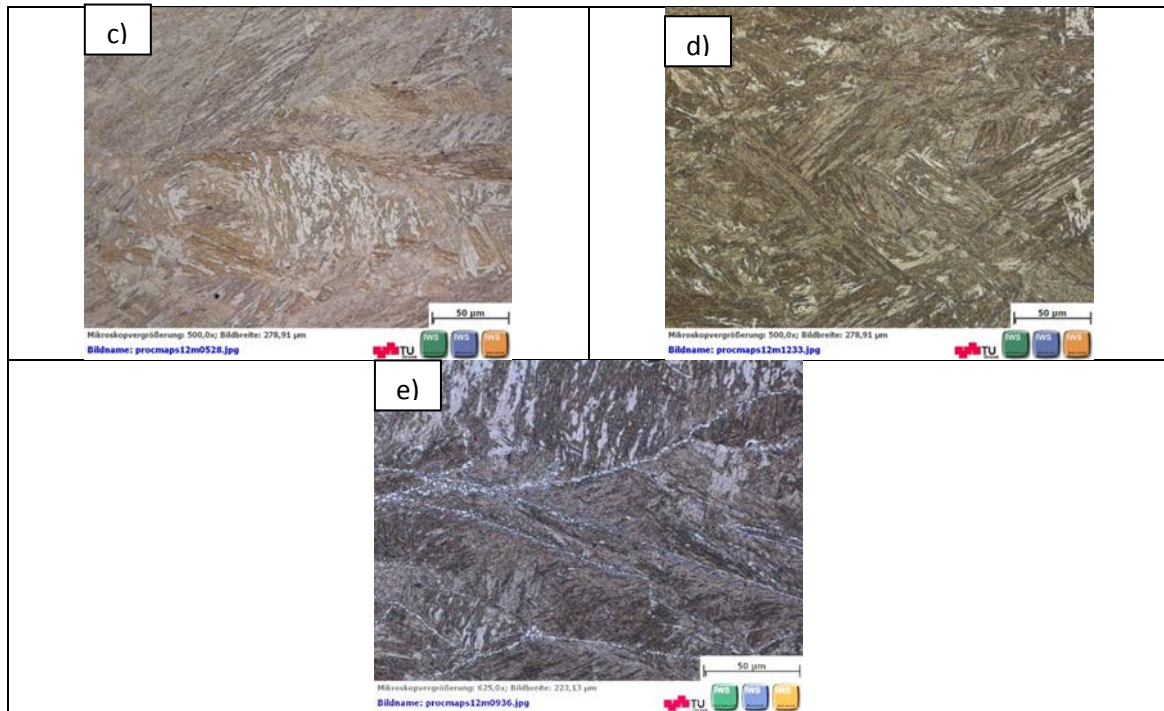
Fig.22. Light optical micrographs showing the microstructure of the material after compression test at 750ºC in the edge (a) strain rate of 0.01s^{-1}, (b) strain rate of 0.1s^{-1}, (c) strain rate of 1s^{-1}, (d) strain rate of 10s^{-1}, (e) strain rate of 80s^{-1}. Magnifiaction 500x

Figure 23 shows that the martensite phase, in dark, predominates over the equiaxed ferrite phase, in white and bainite in light brown. Fragmentation of the prior austenite grains can be observed.
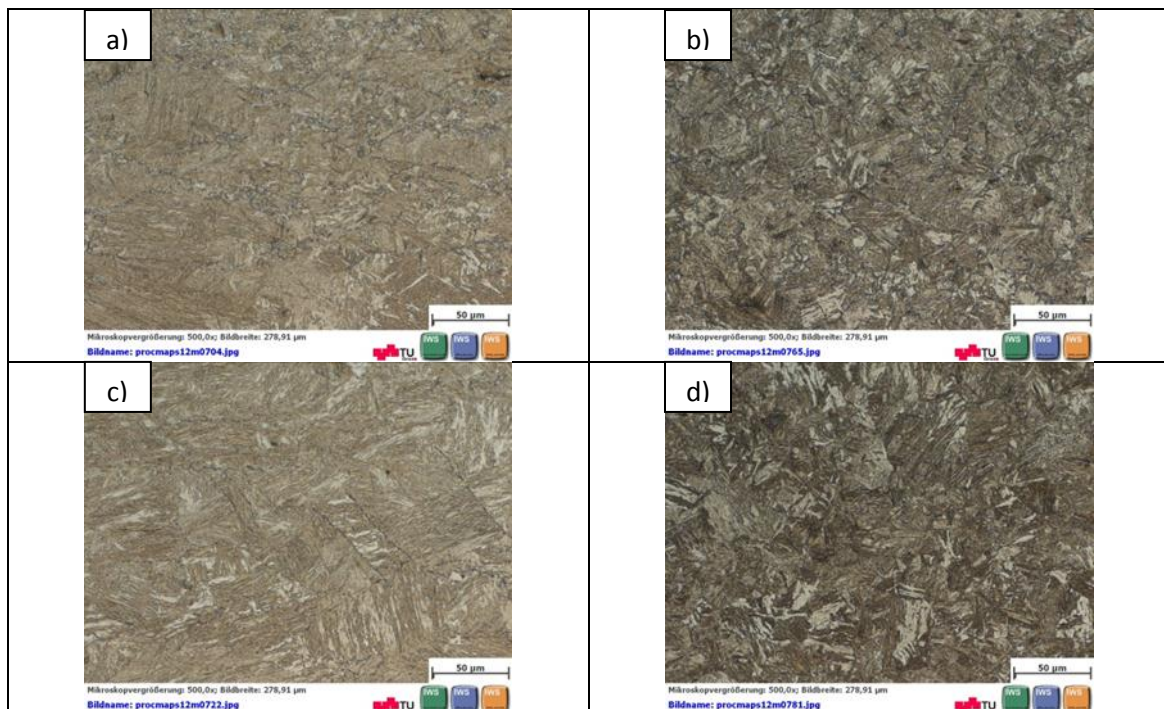
Fig.23. Light optical micrographs showing the microstructure of the material after compression test at 850ºC in the middle (a) strain rate of 0.1s^{-1}, (b) strain rate of 1s^{-1}, and in the edge (c) strain rate of 0.1s^{-1}, (d) strain rate of 1s^{-1}. Magnifiaction 500x

In Figure 24 it can be seen the acicular form of the martensite brown, the bainite in light brown and the equiaxed grains of ferrite in white.

Fig.24. Light optical micrographs showing the microstructure of the material after compression test at 950ºC in the middle (a) strain rate of 0.01s^{-1}, (b) strain rate of 1s^{-1}, (c) strain rate of 10s^{-1}, (d) strain rate of 80s^{-1}. Magnifiaction 500x

The Figure 25 shows the different amount of martensite, in dark, bainite in light brown and equiaxed ferrite and acicular ferrite after deformation at different strain rates at the temperature of 950ºC.
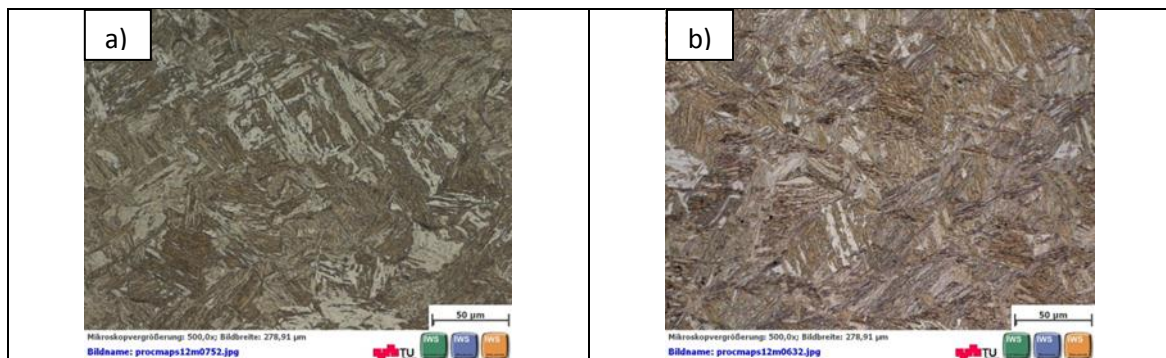
Fig.25. Light optical micrographs showing the microstructure of the material after compression test at 950ºC in the edge (a) strain rate of 0.01s^{-1}, (b) strain rate of 1s^{-1}, (c) strain rate of 10s^{-1}, (d) strain rate of 80s^{-1}. Magnifiaction 500x

The Figure 26 shows the needles of martensite. Also bainite in light brown and acicular ferrite in white can be seen in Figure 26 (b) and (d).
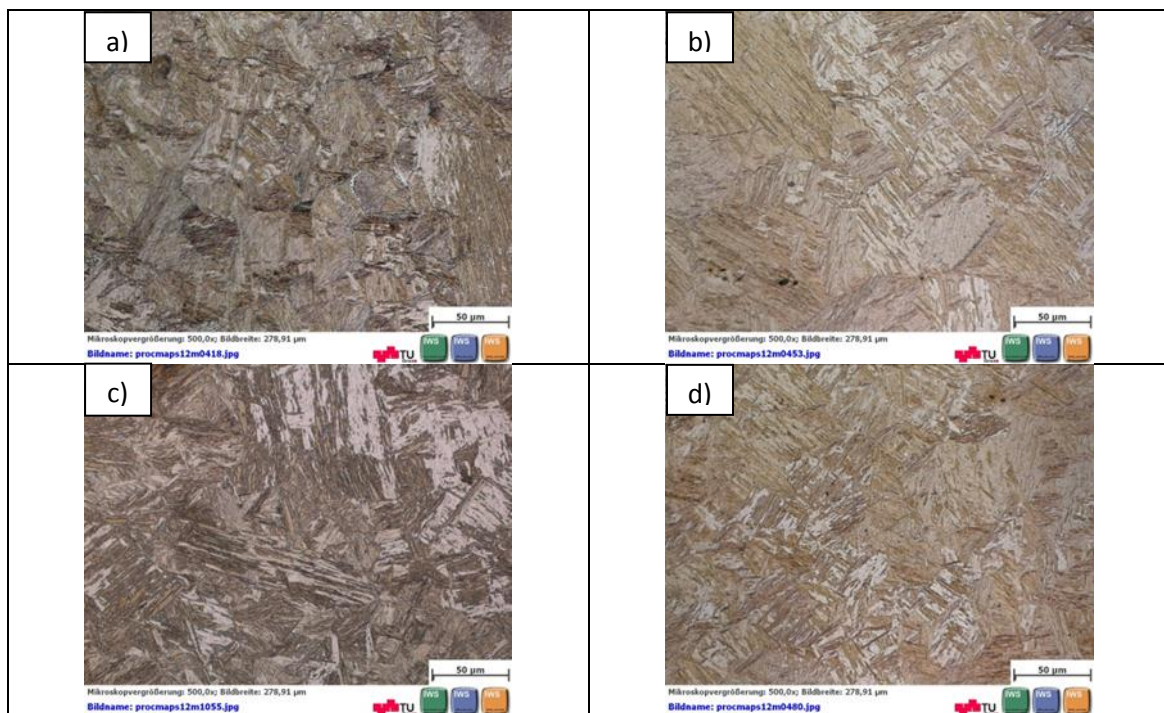
Fig.26. Light optical micrographs showing the microstructure of the material after compression test at 1050ºC in the middle (a) strain rate of 0.01s^{-1}, (b) strain rate of 1s^{-1}, and in the edge (c) strain rate of 0.01s^{-1}, (d) strain rate of 1s^{-1}. Magnifiaction 500x

It can be seen in Figure 27 the grains of martensite in dark, and the amount of acicular ferrite, in white, and the grains of bainite, speccially in the Figure 27 (d) in light brown.
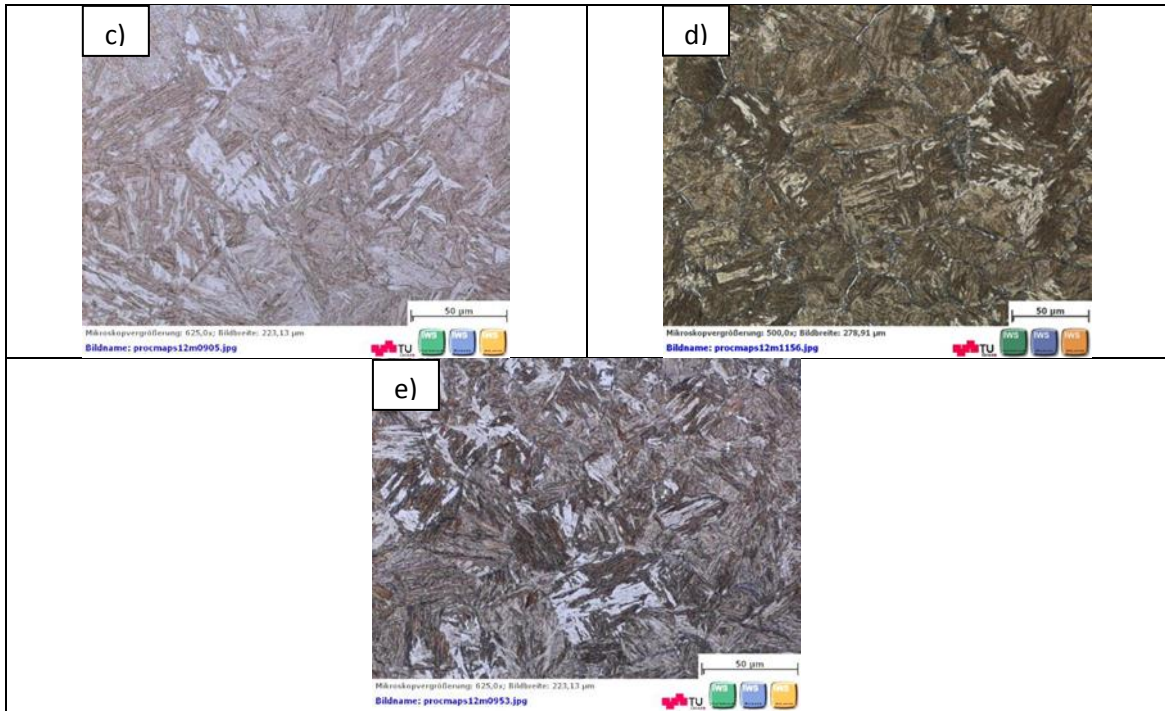
37
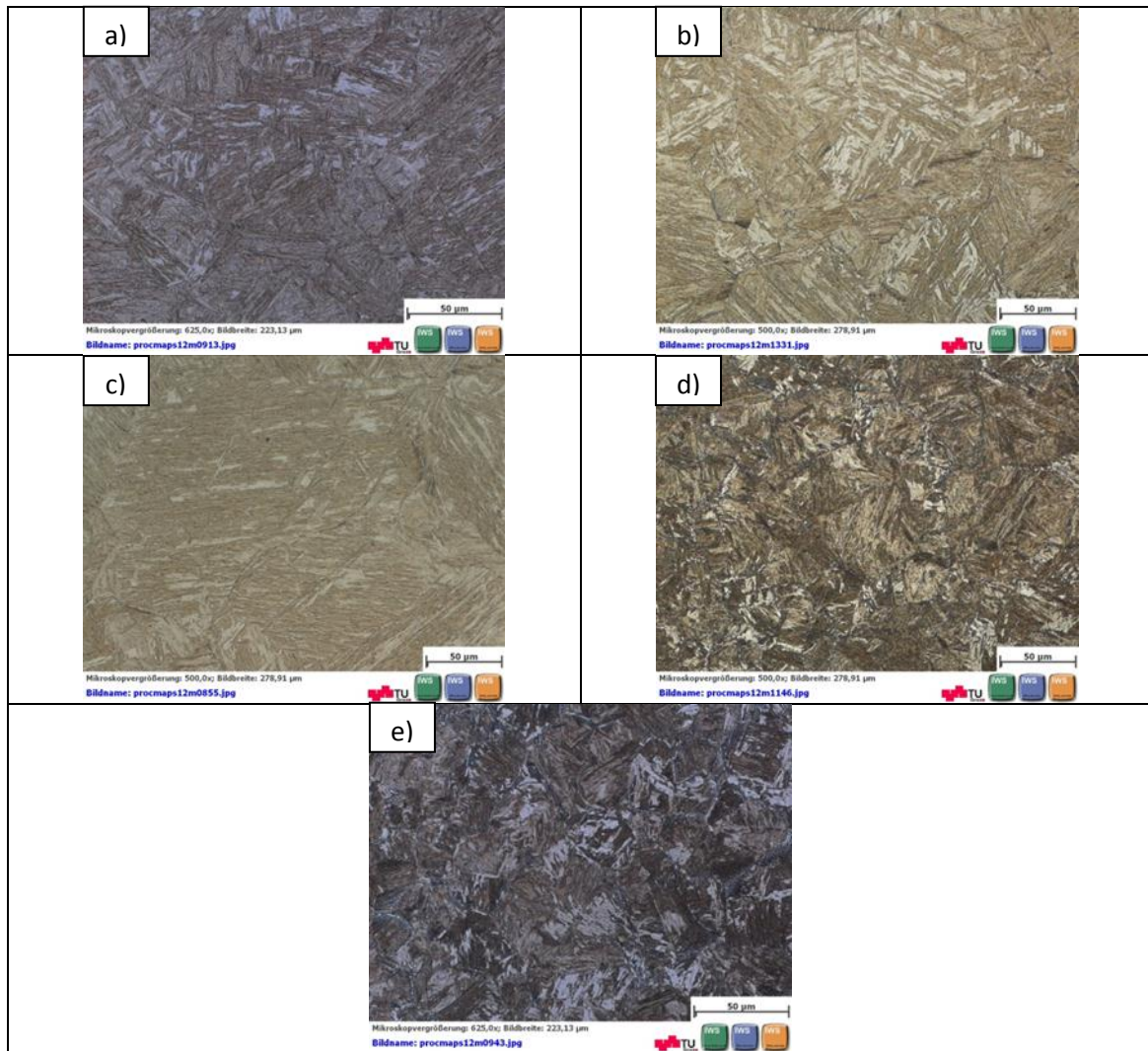
Fig.27. Light optical micrographs showing the microstructure of the material after compression test at 1150ºC in the middle (a) strain rate of 0.01s^{-1}, (b) strain rate of 0.1s^{-1}, (c) strain rate of 1s^{-1}, (d) strain rate of 10s^{-1}, (e) strain rate of 80s^{-1}. Magnifiaction 500x

In the Figure 28 it can be seen the amount of martensite, in dark, the amount of acicular ferrite, in white, and the amount of bainite, in light brown.
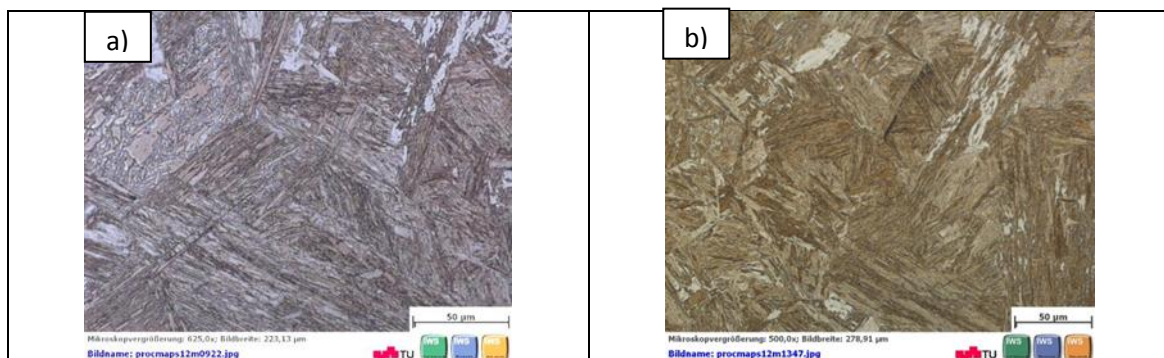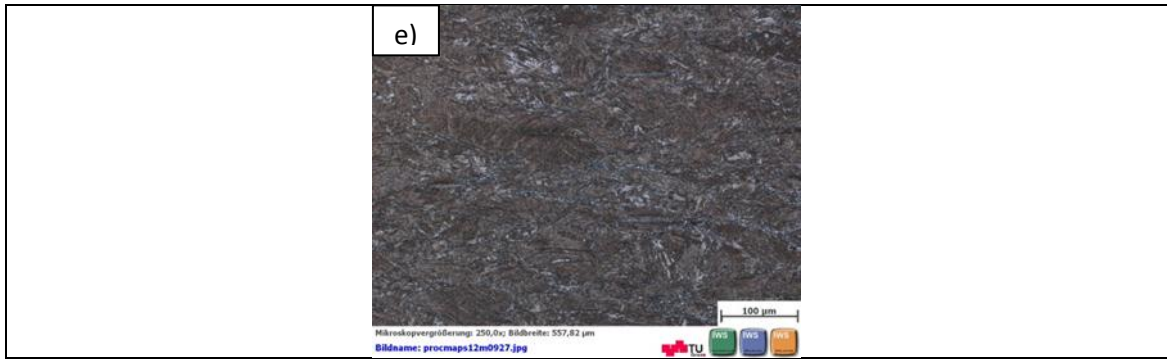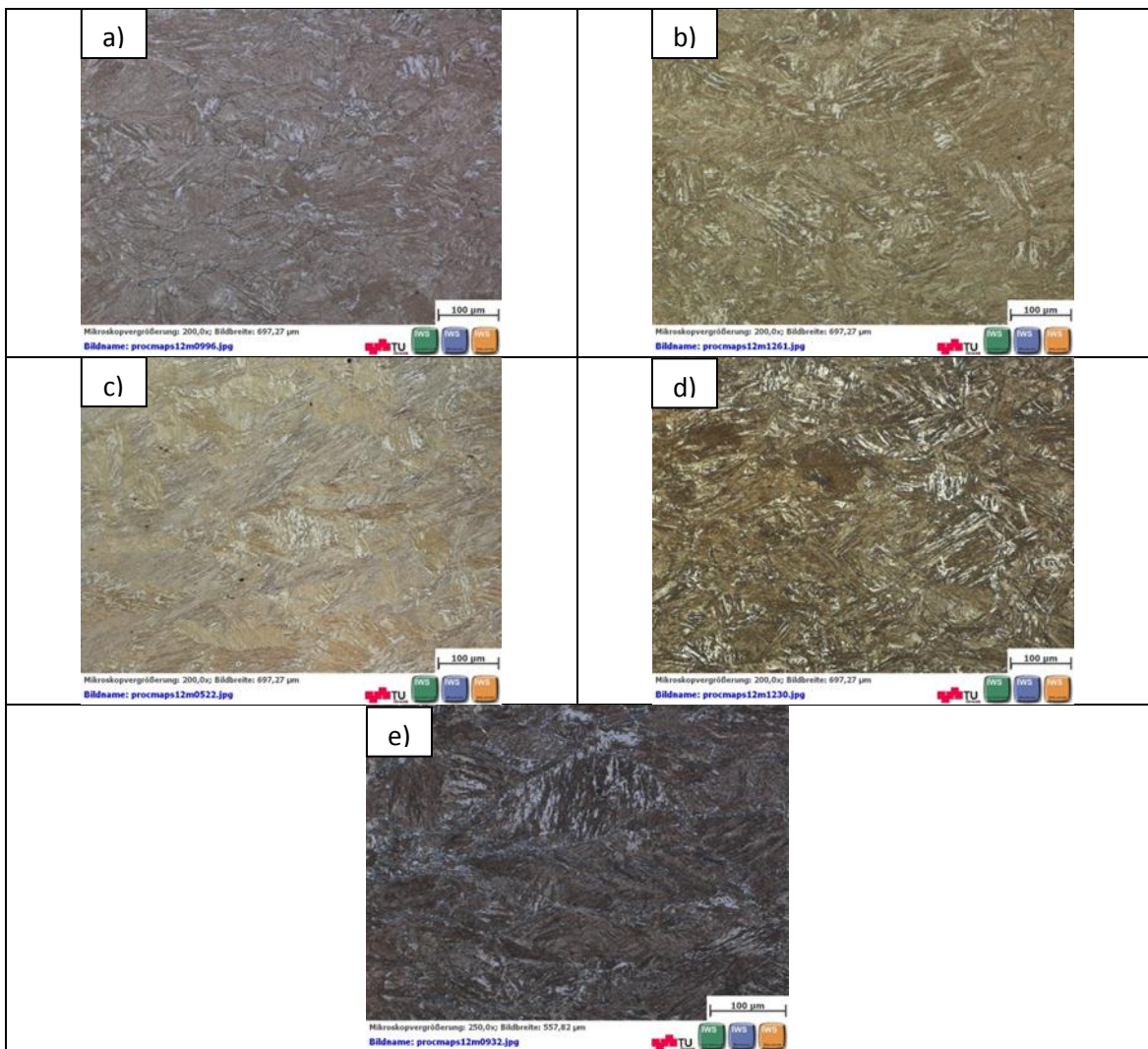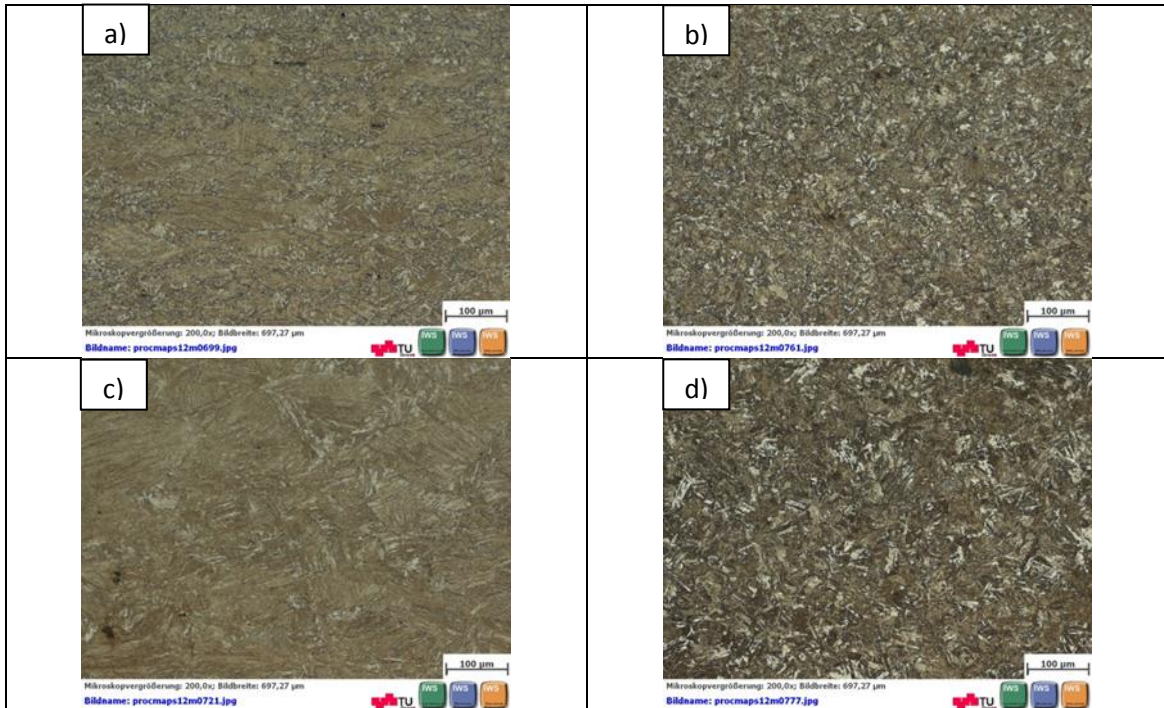
Fig.28. Light optical micrographs showing the microstructure of the material after compression test at 1150ºC in the edge (a) strain rate of 0.01s^{-1}, (b) strain rate of 0.1s^{-1}, (c) strain rate of 1s^{-1}, (d) strain rate of 10s^{-1}, (e) strain rate of 80s^{-1}. Magnifiaction 500x

In Figure 29 there are little grains of equiaxed ferrite at the grain boundaries.
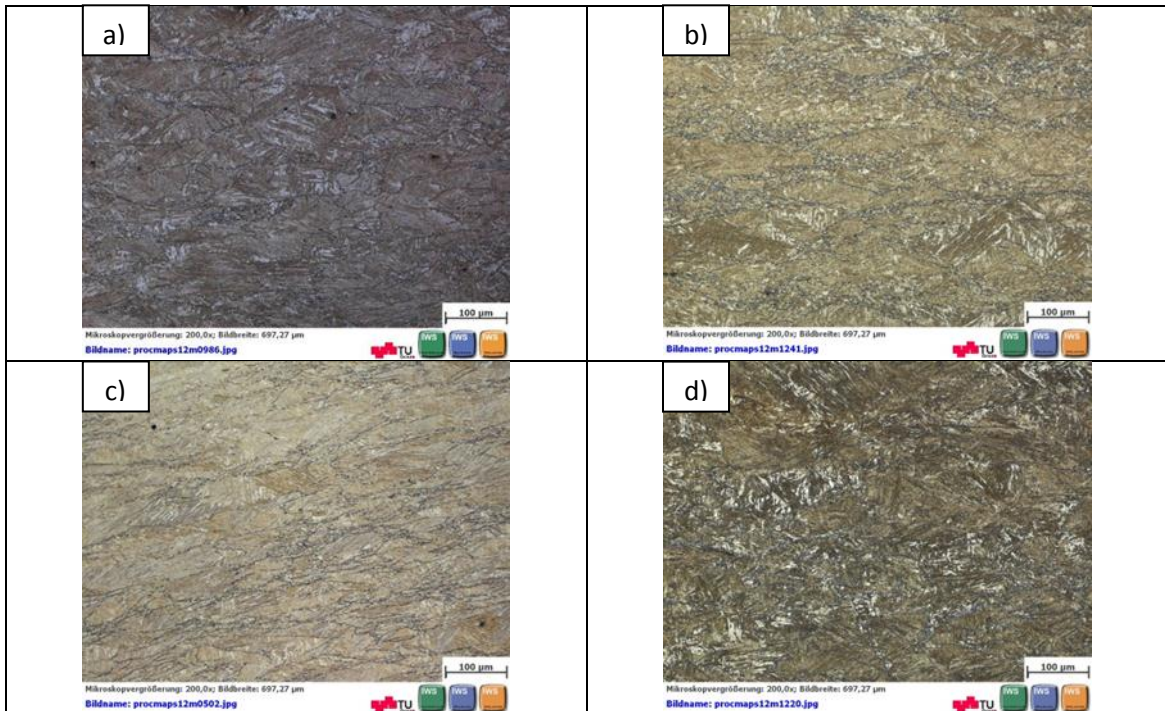
Fig.29. Light optical micrographs showing the microstructure of the material after compression test at 750ºC in the middle (a) strain rate of $0.01s^{-1}$, (b) strain rate of $0.1s^{-1}$, (c) strain rate of $1s^{-1}$, (d) strain rate of $10s^{-1}$, (e) strain rate of $80s^{-1}$. Maginification 200x.

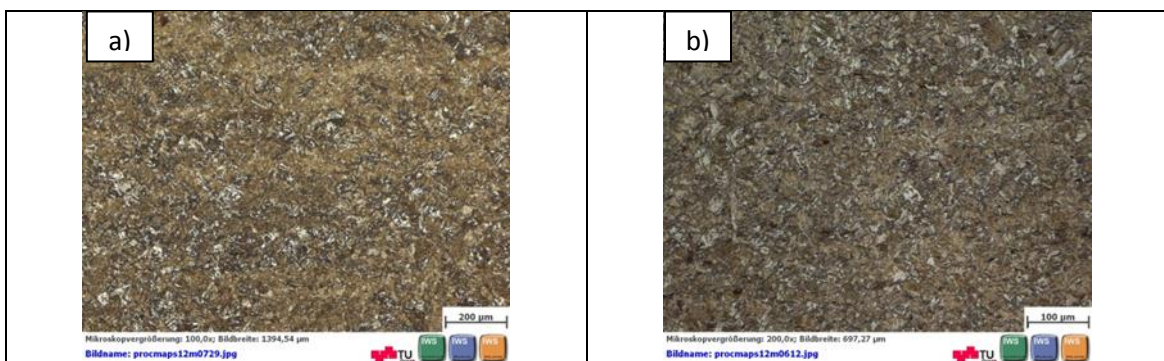In the Figure 30 the acicular structure from the martensite and the equiaxed ferrite can be appreciated.

Fig.30. Light optical micrographs showing the microstructure of the material after compression test at 750ºC in the edge (a) strain rate of 0.01s^{-1}, (b) strain rate of 0.1s^{-1}, (c) strain rate of 1s^{-1}, (d) strain rate of 10s^{-1}, (e) strain rate of 80s^{-1}. Maginification 200x.

The Figure 31 shows the variation of the amount of the martensite, in brown, and the amount of equiaxed ferrite, in white, with different strain rates when the deformation is carried out at the temperature of 850ºC.
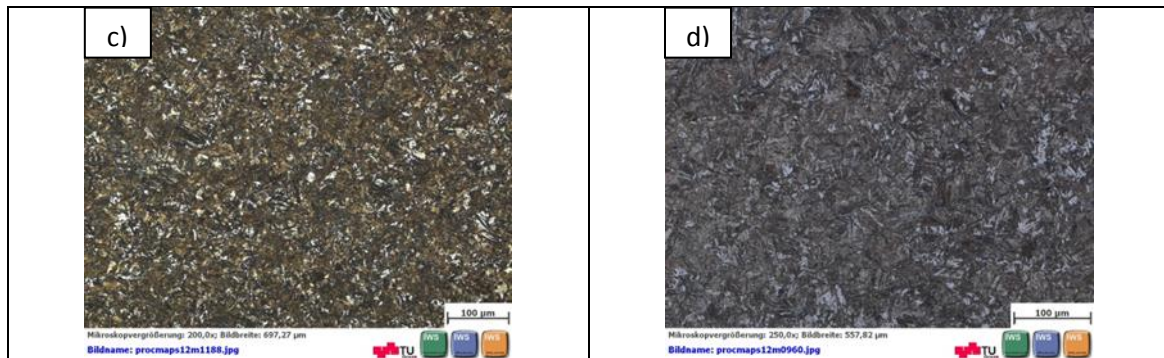

Fig.31. Light optical micrographs showing the microstructure of the material after compression test at 850ºC in the middle (a) strain rate of 0.1s^{-1}, (b) strain rate of 1s^{-1}, and in the edge (c) strain rate of 0.1s^{-1}, (d) strain rate of 1s^{-1}. Magnifiaction 200x.

In Figure 32 the grain of equiaxed ferrite in white and the martensite in brown can be seen. The amount of both phases is similar at the different strain rates.
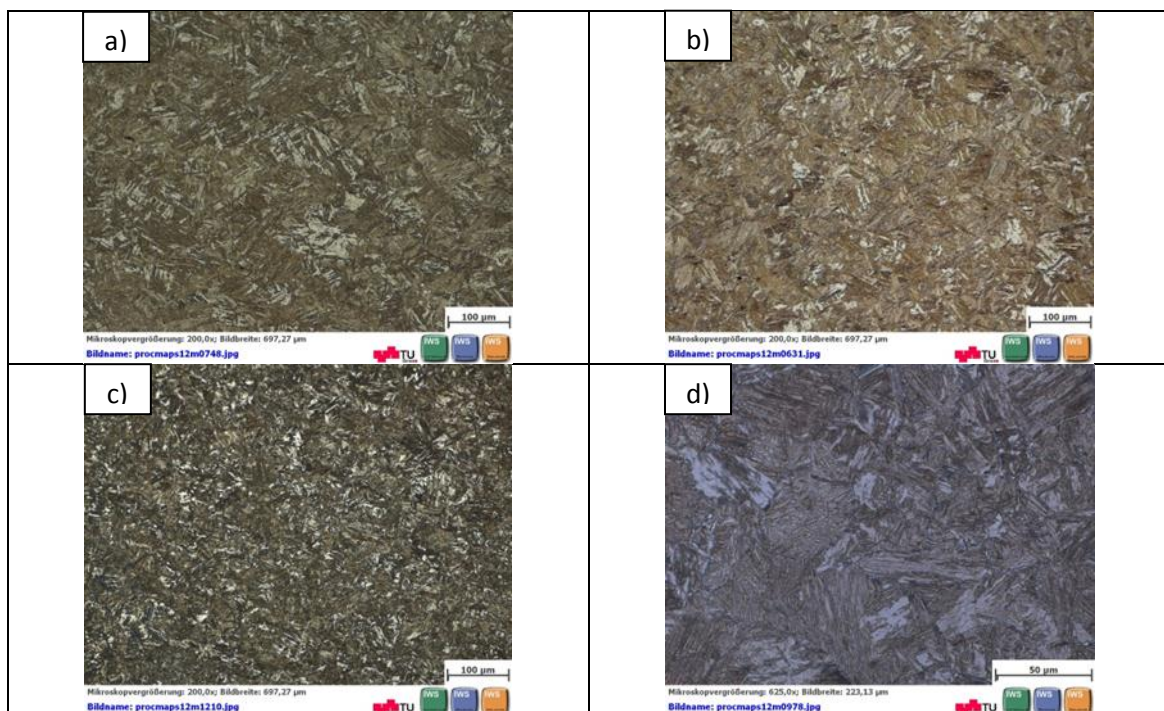

41

Fig.32. Light optical micrographs showing the microstructure of the material after compression test at 950ºC in the middle (a) strain rate of 0.01s^{-1}, (b) strain rate of 1s^{-1}, (c) strain rate of 10s^{-1}, (d) strain rate of 80s^{-1}. Magnifiaction 200x

The Figure 33 shows how the amount of equiaxed ferrite,martensite and bainite changes with the strain rates.
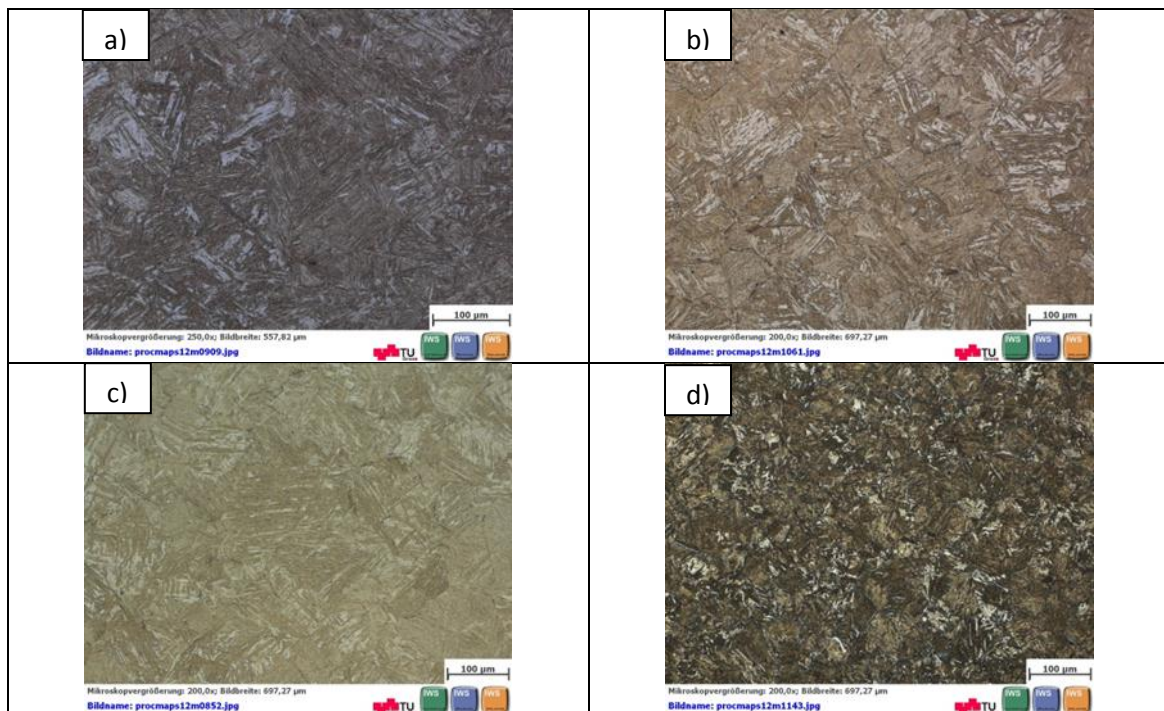

Fig.33. Light optical micrographs showing the microstructure of the material after compression test at 950ºC in the edge (a) strain rate of 0.01s^{-1}, (b) strain rate of 1s^{-1}, (c) strain rate of 10s^{-1}, (d) strain rate of 80s^{-1}. Magnifiaction 200x.

In this case the Figure 34 shows the structure formed for the phases of martensite, acicular ferrite and bainite, light brown.
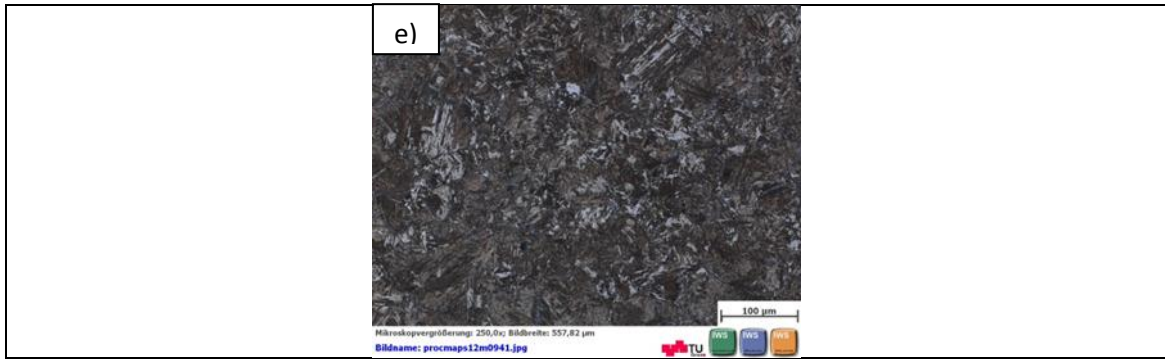
Fig.34. Light optical micrographs showing the microstructure of the material after compression test at 1050ºC in the middle (a) strain rate of 0.01s^{-1}, (b) strain rate of 1s^{-1}, and in the edge (c) strain rate of 0.01s^{-1}, (d) strain rate of 1s^{-1}. Magnifiaction 200x.

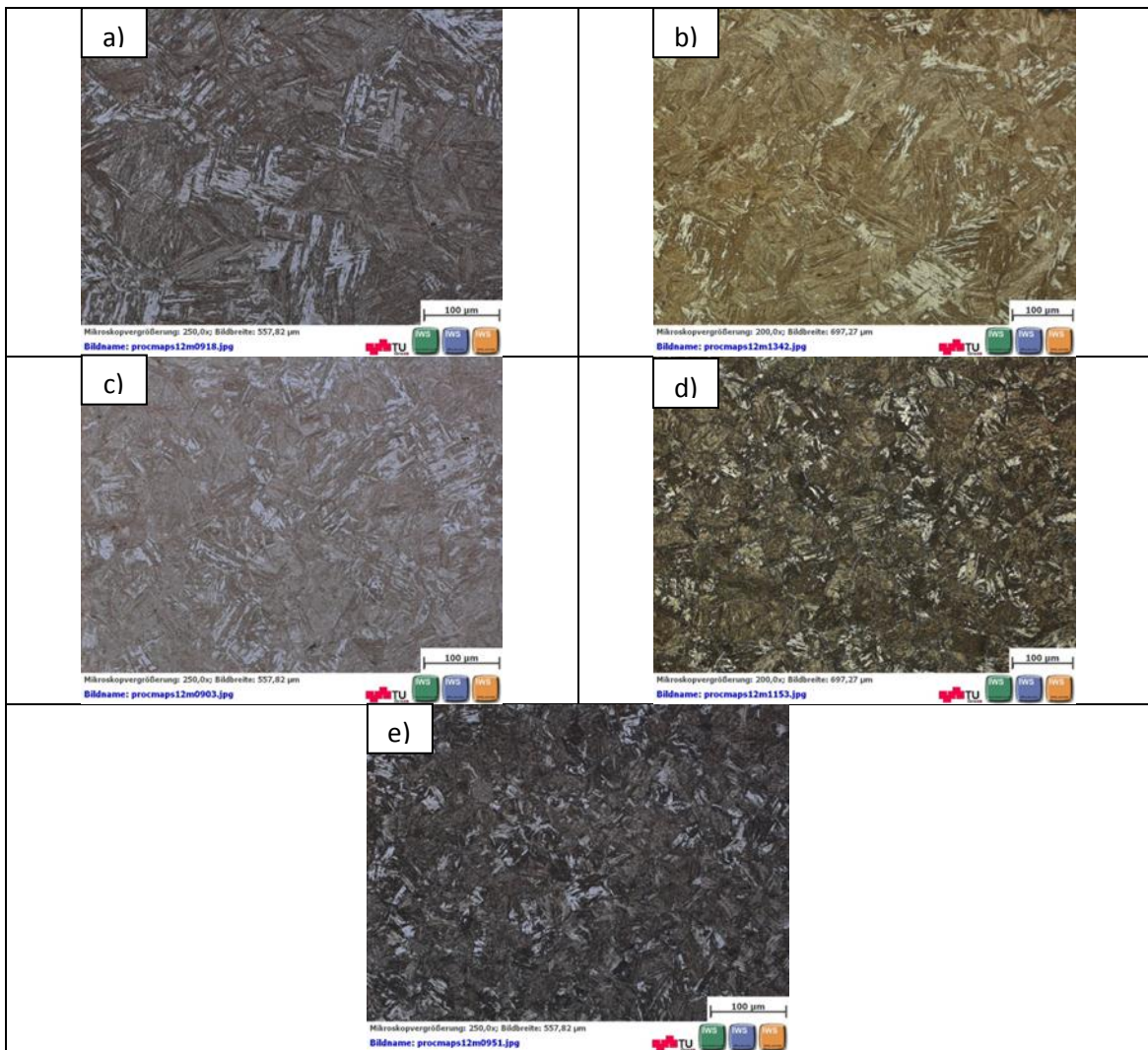Figure 35 similar microstructure than the previous one. The compession was carried out at 1150ºC.

Fig.35. Light optical micrographs showing the microstructure of the material after compression test at 1150ºC in the middle (a) strain rate of 0.01s^{-1}, (b) strain rate of 0.1s^{-1}, (c) strain rate of 1s^{-1}, (d) strain rate of 10s^{-1}, (e) strain rate of 80s^{-1}. Magnifiaction 500x.

The Figure 36 shows the amount of the different phases that form the structure. These phases are martensite, dark brown, acicular ferrite in white and bainite in light brown.
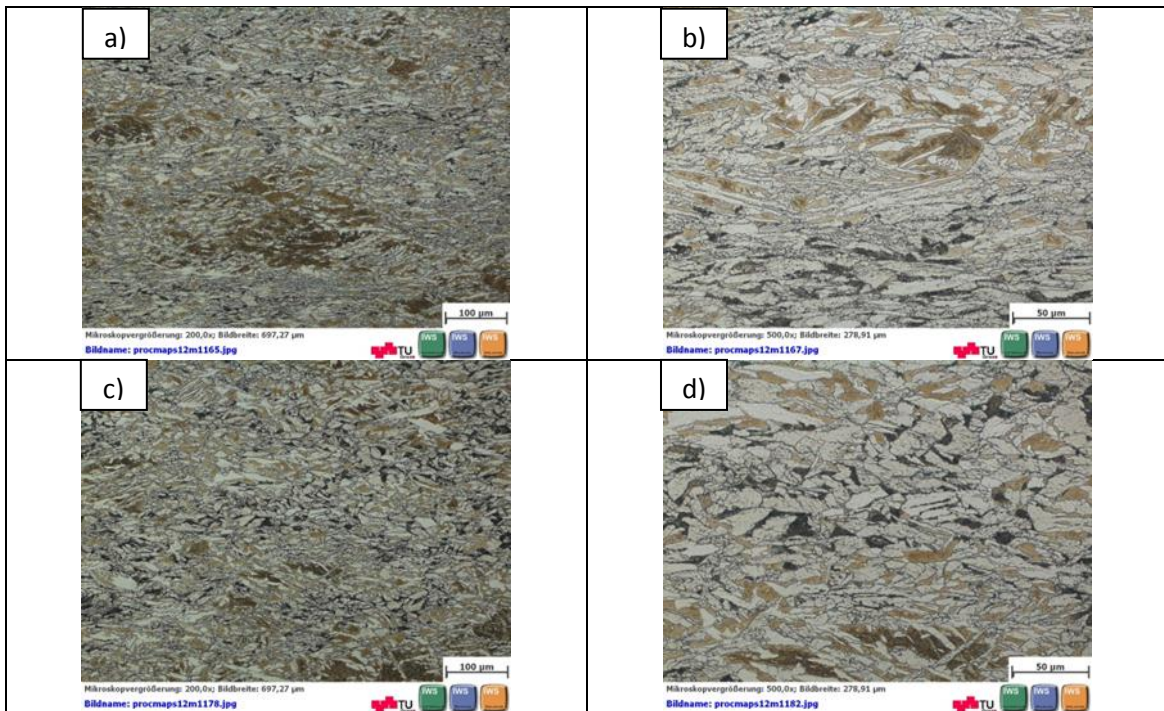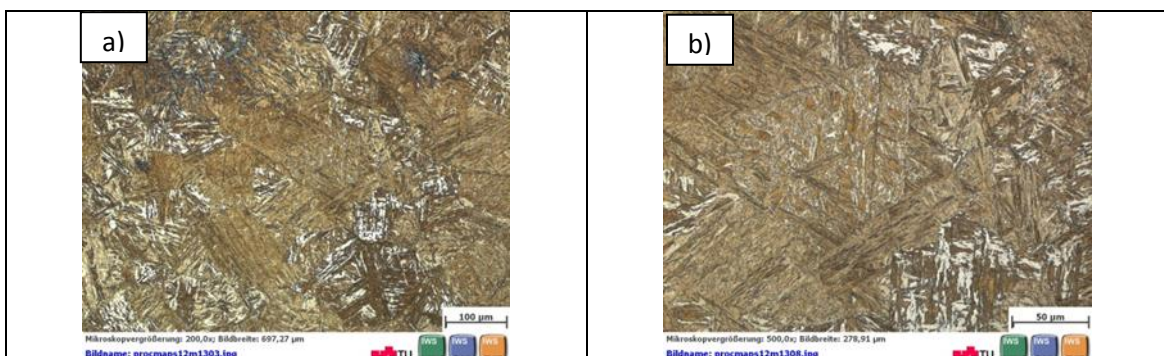
Fig.36. Light optical micrographs showing the microstructure of the material after compression test at 1150ºC in the edge (a) strain rate of 0.01s^{-1}, (b) strain rate of 0.1s^{-1}, (c) strain rate of 1s^{-1}, (d) strain rate of 10s^{-1}, (e) strain rate of 80s^{-1}. Magnifiaction 200x.

In Figure 37 the structure after compression tests carried out at 650ºC at different strain rates can be seen. The structure is different to the previous and equiaxed ferrite,white, bainite,light brown and perlite in black can be seen.

Fig.37. Light optical micrographs showing the microstructure of the material after compression test at 650ºC in the middle strain rate of 0.01s^{-1} (a)magnification x200 and , (b) magnification x500 and in the edge (c) magnification x200 and (d) magnification 500x.

The Figure 38 shows the microstructure of the material after a heat treatment without compression at 750ºC. The martensite in dark brown, the bainite in light brown and ferrite in white can be seen.
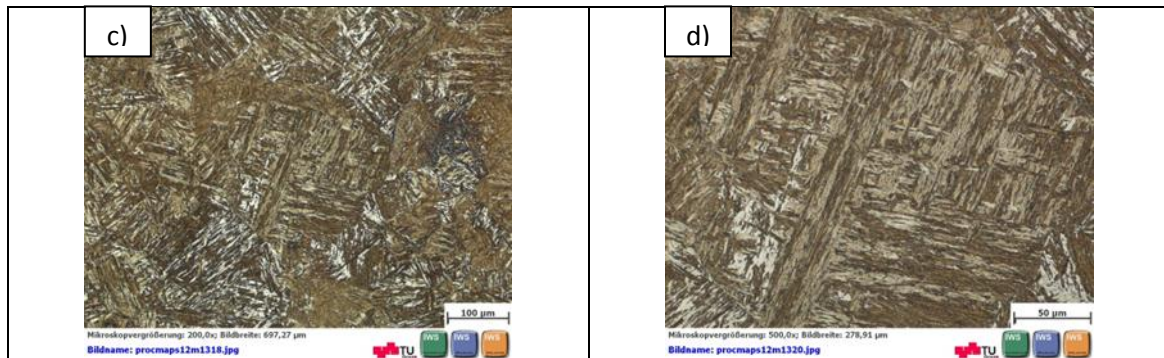
Fig.38. Light optical micrographs showing the microstructure of the material after a heat treatment without deformation at 750ºC in the middle, (a)magnification x200 and , (b) magnification x500 and in the edge (c) magnification x200 and (d) magnification 500x.

In Figure 39 the different amount of the phases, martensite, bainite and ferrite that constitute the structure after the compression test carried out at 1050ºC and different strain rates can be seen.
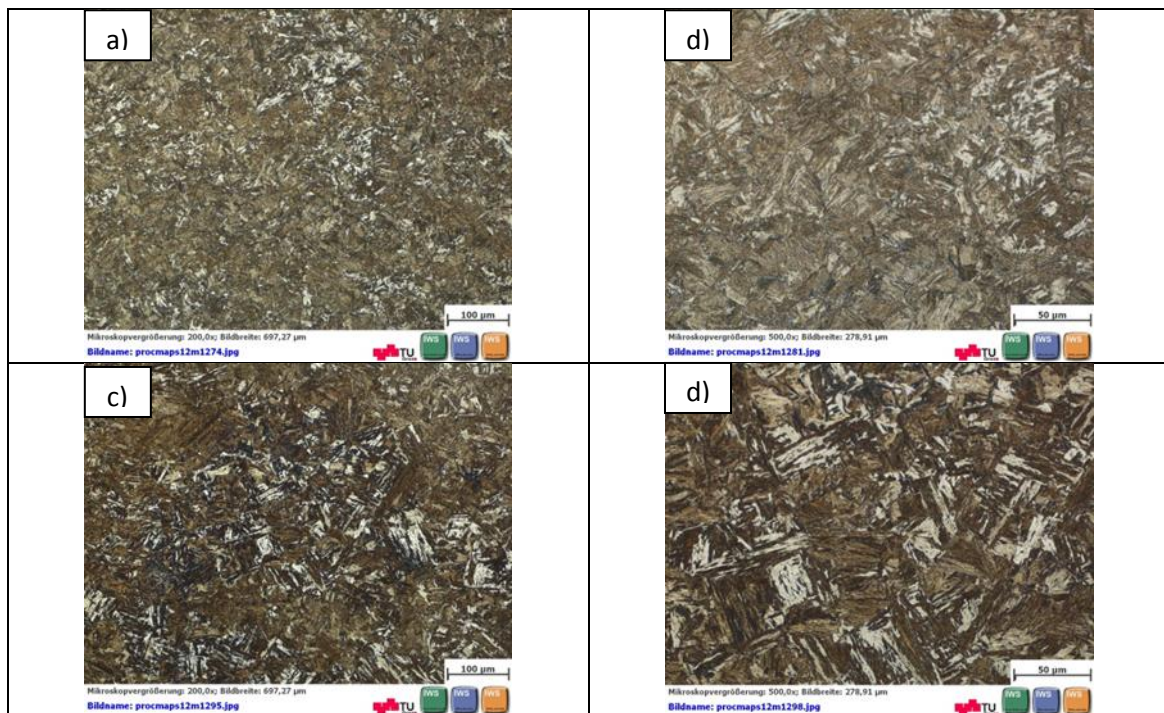
Fig.39. Light optical micrographs showing the microstructure of the material after heating up the sample to 1050ºC, cooling down until 950ºC with 1 K/s and at this temperature the compression test is carried out, in the middle(a)magnification x200 and , (b) magnification x500 and in the edge (c) magnification x200 and (d) magnification 500x.

5. DISCUSSIONS

5.1. PHASE TRANSFORMATONS

The variation of the relative change of length as a function of temperature *(ΔL/L0=f(T))*is shown in the dilatometric curve of Fig.13.

5.1.1. HEATING

The Ac_1 and Ac_3 critical temperatures are, respectively, the start and finish temperature of the change of phase from ferrite plus perlite to austenite. In this case the average temperature for the Ac_1 is 813 ±6°C for all the samples since they are heated at the same heating rate. This result depends on the composition and starting microstructure of the sample.

The Ac_2 temperature indicates when the ferromagnetic transformation occurs. In this case the average temperature is 753°C with values ranging 5°C above to 2°C below, so at this temperature the steel changes from ferromagnetic to non-ferromagnetic.

Ac_3 is the point when the change of phase is completed, the average temperatures are 875°C and the range is 6°C below and 3°C above.

5.1.2. COOLING

The Ar_3 and Ar_1 critical temperatures correspond, respectively, to the start and finish temperatures of the non-isothermal decomposition of austenite into ferrite plus pearlite. In the case of cooling rate equal to 1K/s, the transformation took place slowly obtaining as final products, ferrite, bainite and perlite.

The average temperature when the transformation starts, Ar_3, is 724°C and the values are in a range is 4°C above and 3°C below. In the case of cooling with helium, the cooling rate is 136°C/s and the dilatometry curve shows that two different phase transformations occur when cooling from 1000°C. Metallographic examination shows that the final microstructure obtained after cooling with a high rate is composed of bainite and martensite. Bainite is formed at higher temperatures than martensite, so the first volume expansion displayed on the curve corresponds to the transformation of austenite into bainite, whereas the volume expansion shown at lower temperatures corresponds to the transformation of austenite into martensite.

The pictures of the Figure 19(a), (c) and (e) correspond to sample which were undergone a heat treatment with cooling ate of 1 K/s, so the equilibrium is attained and the phases obtained are ferrite, the white one, and pearlite, the black one. When the sample is heated up to 1150°C (e), the austenite grain size is bigger than when the samples is heated up to 1000°C, (a) and (c). In the pictures (b), (d) and (f) of Figure 19 the samples were cooled with helium at 136 K/s. Thus, the equilibrium is not achieved and the final phases are martensite, bainite and ferrite. The austenite grain size when the sample is heated up to 1150°C (f) is bigger than when the samples are heated up to 1000°C (b) and (d).

The etching with Beraha I resulted more colorful pictures and it was possible to distinguish between the ferrite, white, the martensite, black or dark brown and sometimes blue, and the bainite and tempered martensite, light brown [61]. These pictures show that after the quenching, that not the whole austenite transforms into martensite, there are bainite and ferrite too, as observed in the dilatometry curves, especially for the short time / low temperature austenitization treatment.

Thus, austenite grain size developed during austenitization treatment plays an important role in the phase transformation during cooling: large grains promote the formation of 100% of martensite during fast cooling, while small austenite grains (obtained at short austenitization times and/ or low temperatures) result in the additional formation of bainite. The "nose" of bainite formation in the CCT curve moves to the left side (to shorter times or faster cooling rates) by decreasing the grain size.

After hot deformation acicular ferrite or bainite can be formed cooling since the "nose" in CCT curve should move to the left due to austenite grain refinement by grain fragmentation at low temperatures and by dynamic recovery at high temperatures and due to dislocations density increment.

5.2. FLOW BEHAVIOUR AND DEFORMATION MECHANISMS

The flow curves of the Figure 14 showed that:

a) At the same strain rate, the yield stress is increasing with decreasing the temperature.
b) The yield stress is increasing with increasing the strain rate.
c) When the compression is carried out at the same temperature, the yield stress is increasing with increasing the strain rate.

At lower temperatures, after hardening due to deformation, steady state is achieved. Fragmentation of prior austenite is observed and formation of strain induced. Both result in flow softening. Additional softening can occurs due to dynamic recovery of the ferritic phase.

When the sample has undergone a compression test at 750°C, small ferrite grains appear in the grain boundaries as it can be seen in Figure 40. This ferrite is strain induced ferrite which is formed during the compression tests and not during the cooling. A detail of this feature ia shown in Figure 40.
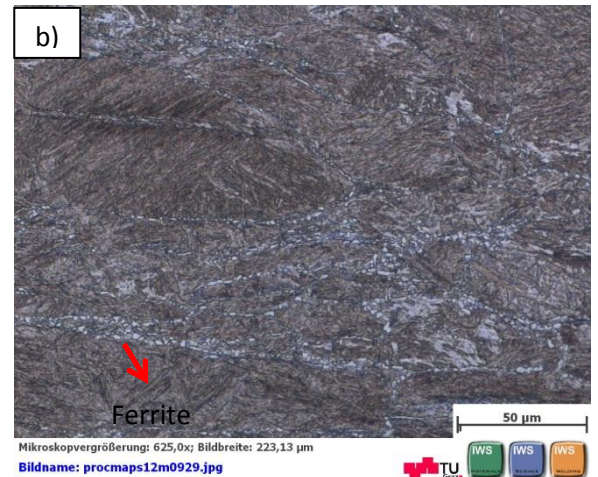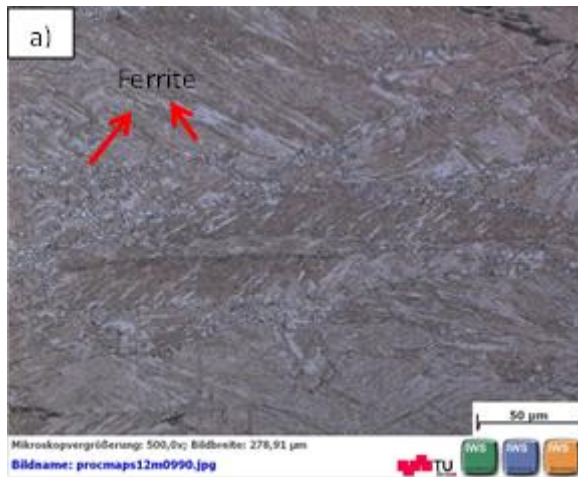
Fig.40. This figure shows the ferrite grains after compression tests carried out a 750ºC (a) 0.01 s^{-1} and (b) 80 s^{-1}

In Figure 41 deformation bands can be seen. It occurs at temperatures below 950°C when the compression test is carried out at high strain rates.

Fig.41. Deformation bands in a compression test carried out at 750ºC. This picture was taken in the edge of the sample.

The Figure 14 shows that at high temperatures, above 950°C, and at low strain rates, after the maximum value of stress, the value of the stress decreases until a constant value, achieving the steady state. This indicates that under these conditions the microstructural mechanism which dominates is the dynamic recrystallization also observed in the refinement of the prior austenite grains. It was also observed that new recrystallized grains formed during hot deformation are equiaxed, and their size depend on both strain rate and temperature.

In this range of temperatures, the grain size increases with decreasing strain rate and increasing the temperature. This can be seen in the Figure 42 in which grain boundaries are plotted.

49
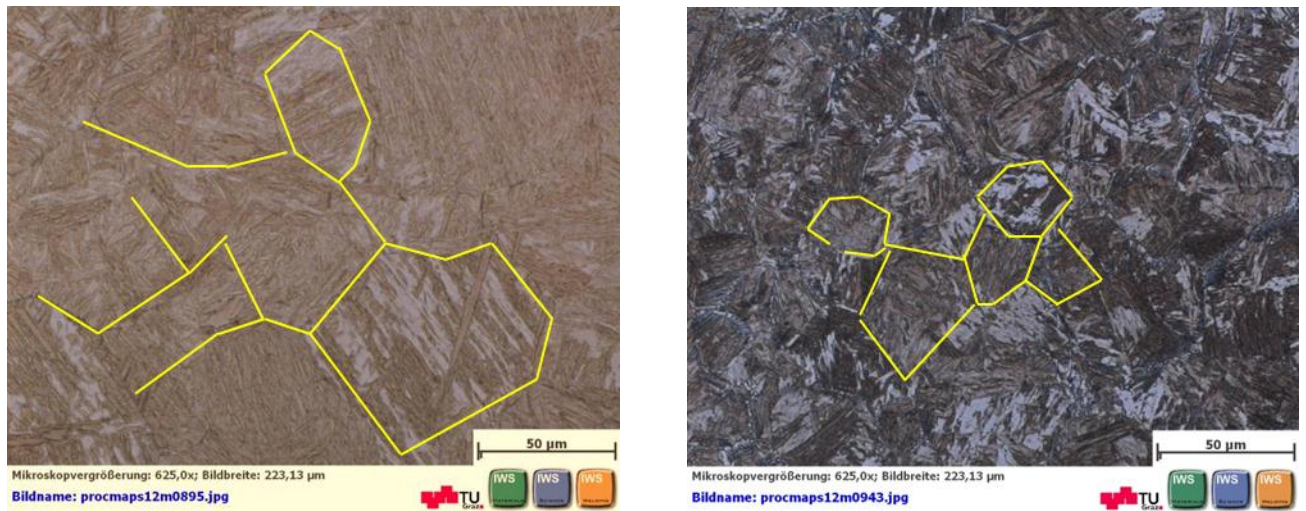
Fig.42. This figure shows the grain size after compression tests carried out at 1150ºC, (a) 1 s^{-1} and (b) 80 s^{-1}.
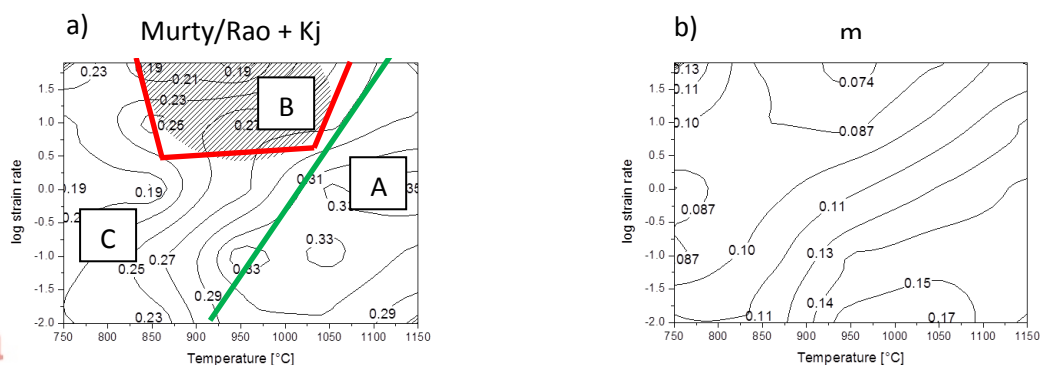
5.3. PROCESSING MAPS

The main aims of the project are the study of the deformation behaviour of the microalloyed steel by means of processing maps and to compare the prediction with the developed microstructure.

The processing maps as well as the m maps can be divided into three domains as shown in Figure 43.

The area A is a safe area with high values of efficiency and m which increase by decreasing the strain rate and increasing the temperature. This can be related to recrystallization of austenitic phase.

The region B indicates low values of efficiency and m. Furthermore, instability is predicted, by k_j, which can be related to adiabatic flow. The tests carried out show that at temperatures between 850ºC and 1050ºC and high strain rates, there is an increasing of the temperature of 10-15ºC after the compression occurs. So this is indicates the adiabatic flow.

In C area there is not any instability but both efficiency and m values are low or middle, so is not an interesting zone to carry out deformations. The values are higher at the lowest strain rates where strain induced ferrite is formed, and at high strain rates due to fragmentation of the austenite grains.

50

Fig.43. Processing map of Murty and Rao with the instability map of K_j and the m map at strain of 0.3

The highest values in the m map are in the same area than in the Murty and Rao map, and the lowest values are in the area in which the Murty and Rao map predicts instability, but the m model says that instability occurs when the m value is lower than zero [1].

At a strain of 0.4, 0.5 and 0.6 the areas related to DRX of austenite are more or less the same size than at a strain of 0.3. Furthermore the area which predicts instability decreases or remain the same for 0.4, 0.5 and 0.6 in comparison with the area at a strain of 0.3

There are other processing maps based on different criteria.

In Figure 16 there are another two different processing maps. The Figure 16 (c) represents the processing map calculated with the efficiency criteria proposed by Murty and Rao and also the instability map is calculated with the Murty and Rao criteria. In Figure 16 (d) the processing map is calculated by the Prasad criteria and the efficiency is also calculated according the Prasad criteria. The efficiency has the same distribution than the m map because the eta of Prasad is directly related with m as it is possible to see in equation (6). The instability is located at low-middle temperatures and low-middle strain rates

The Murty and Rao plus $k_{Murty\ and\ Rao}$ does not fit for this material and these conditions, because it predicts instability in areas that the flow curves and the microstructure does not show these instabilities.

The processing map done according the Prasad criteria the instability area does not fit to the instability that the flow curves and the pictures of the microscopy predict. So this processing map is not the better map for this material and these conditions.

The best model according these conditions is the Murty/Rao model with K_j equation to calculate the instability because the deformation mechanisms that appear in the pictures of the LOM fit very well to the distribution of the efficiency of this map and also the instability.

6. SUMMARY AND CONCLUSIONS

The deformation mechanism of a microalloyed steels was studied by means of hot compression tests in a wide range of temperature and strain rates, dilatometry and metallography. Additionally some phenomelogical models were applied to study formability of the material. The following can be summarized and concluded.

It was shown that the *Murty/Rao plus K_j* model and the m maps correlate well with the microstructure, although no instability is predicted by m. Three deformation domains could be identified:

A. Temperature above 950° shows the largest η and m values, increasing by increasing the temperature and decreasing the strain rate, and is related to the DRX of the austenite. This is the range of hot deformation, instabilities are not predicted.
B. *When strain rates are high (1-80/s) and the temperature is low, the efficiency and m values are low-moderate and there is instability when the temperatures approach to 950°. Instabilities predicted by k_J should be related to adiabatic flow behavior.*
C. When the strain rates are low (0.01-1/s) and the temperature is low (<950°C) the values of the efficiency are low-moderate. The region is stable. Observing the microstructure, formation of strain induced ferrite at low temperatures can be seen.

7. REFERENCES

[1] A.Al Omar, J.M. Prado, *Aplicaciones de los mapas de procesado en la optimización de los parámetros de un proceso de conformado en caliente* 1996.

[2] Jonas, J.J, Sellars, C.M, Tegart, W.J. McG. Metall. Rev. 14, 1969: 1-12.

[3] Sellars, C.M, Tegart, W.J. McG., Mém. Scientifiq. Rev. Métall. LXIII (9), 1996: 731-746.

[4] Frost, H.J., Ashby, M.F. Deformation-mechanism maps. The plasticity and creep of Metals and Ceramics. Ed. Pergammon Press, Oxford (U.K.) 1982: chapters 1-5.

[5] Garofalo, F., Trans. AIME, 227, 1963:351-356.

[6] Raj, R. Metall. Trans.A, 12, 1981: 1089.

[7] A.Al Omar, J.M. Prado, I,Alcelay, *Criterios de predicción de inestabilidades plásticas en procesos de conformado en caliente.*

[8] Y.V.R.K. Prasad. Metal. Trans. A27 (1996) 235-236

[9] C. Poletti a,∗, H.P. Degischer a, S. Kremmerb, W. Marketz, Processing maps of Ti662 unreinforced and reinforced with TiC particles according to dynamic models, Materials Science and Engineering A 486 (2008) 127–137.

[10] S.V.S.N. Murty, B.N.Rao. Mater. Sci. Letters 17 (1998), 1203 – 1205

[11] www.omega.com

[12] Ziegler.H. Progress in solid mechanica, ed. I.N.Sneddon and R.Hill. 1963:93.

[13] S.V.S. Narayana Murty, B. Nageswara Rao, J. Mater. Sci. Lett. 17 (1998) 1203–1205

[14] C. Poletti, J. Six, M. Hochegger, H. P. Degischer and S. Ilie STEEL RESEARCH INTERNATIONAL 82-6 (2011) 710–718

[15] R.D. Doherty, D.A. Hughes, F.J. Humphreys, J.J. Jonas, D.J. Jensen, M.E. Kassner, W.E. King, T.R. McNelley, H.J. McQueen and A.D. Rollett, Mater. Sci. Eng. A, Vol. 238 (1997), pp. 219-274.

[16] R.A.P. Djaic and J.J. Jonas, J. Iron Steel inst., Vol. 210 (1972), pp. 256-261.

[17] A.J. DeArdo, "Fundamental Aspects of the Physical Metallurgy of Thermomechanical Processing of Steel", THERMEC-88: International Conference on Physical Metallurgy of Thermomechanical Processing of Steels and Other Metals, Tokyo, Japan, 1988, pp. 20-29.

[18] D. Hull and D.J. Bacon, "Introduction to Dislocations, Third Edition", Pergamon Press Ltd , Headington Hill Hall, Oxford OX3 0BW, England, 1984, pp. 230.

[19] F.J. Humphreys and M. Hatherly, "Recrystallization and related annealing phenomena", Elsevier Science Ltd , The Boulevard, Langford Lane, Kidlington, Oxford OX5 1GB, UK, 2004.

[20] Linda Bäcke, Modeling the Microstructural Evolution during Hot Deformation of Microalloyed Steels, Doctoral thesis pp 10-12

[21] P.D. Hodgson, Mater. Forum, Vol. 17 (1993), pp. 403-408.

[22] F.J. Humphreys, Materials Science Forum, Vol. 467-470 (2004), pp. 107-116.

[23] C.M. Sellars, "Microstructure modeling in hot deformation", Thermo-Mechanical Processing in Theory, Modelling & Practice [TMP] exp 2, Stockholm, Sweden, 1997, pp. 35-51.

[24] C.M. Sellars, "The Physical Metallurgy of Hot Working", Hot Working and Forming Processes, Sheffield, UK, 1980, pp. 3-15.

[25] W.P. Sun, M. Militzer, E.B. Hawbolt and T.R. Meadowcroft, "Austenite grain refinement and growth during the thermomechanical processing of steels", Hot Workability of Steels and Light Alloys-Composites; Montreal, Quebec; Canada, 1996, pp. 285-292.

[26] R.A.P. Djaic and J.J. Jonas, J. Iron Steel inst., Vol. 210 (1972), pp. 256-261.

[27] T. Sakai and J.J. Jonas, Acta Metall., Vol. 32 (1984), pp. 189-209

[28] E.I. Poliak and J.J. Jonas: *ISIJ Int*., 2003, 43, 684.

[29] R. Kapoor, B. Paul, S. Raveender, I. Samajdar and J.K. Chakravartty: *Metall. Mater. Trans. A*, 2009, 40, 818-827

[30] *M. Shaban and B. Eghbali, Characterization of Austenite Dynamic Recrystallization under Different Z Parameters in a Microalloyed Steel, J. Mater. Sci. Technol., 2011, 27(4), 359-363.*

[31] J.E. Burke, D. Turnbull, Prog. Metal Phys. 3 (1952) 220

[32] S.B. Davenport , R.L. Higginson, Strain path effects under hot working: an introduction, Journal of Materials Processing Technology 98 (2000) 267±291

[33] H. Hu, Trans. Metall. Soc. AIME 224 (1962) 75.

[34] J.W. Martin, R.D. Doherty, The Stability of Microstructure in Metals, Cambridge University Press, Cambridge, 1976.

[35] J.C.H. Li, J. Appl. Phys. 33 (1962) 2958.

[36] P.A. Beck, P.R. Sperry, J. Appl. Phys. 21 (1950) 150.

[37] I.L. Dillamore, H. Katoh, Metals Sci. 8 (1974) 73.

[38] W.B. Hutchinson, E. Nes, Annealing Processes Ð Recovery, Recrystallisation and Grain Growth, 1986, pp. 107±122.

[39] J. Hjelen, E. Nes, in: J.S. Kallend, G. Gottstein (Eds.), Eighth International Conference on Textures of Materials (ICOTOM 8), 1988, 597 pp.

[40] J. Hjelen, R. érsund, E. Nes, Acta Metall. 39 (1991) 1377

[41] E. Nes, W.B. Hutchinson, in: Proceedings of the 10th International Risù Symposium, 1989, 233 pp.

[42] E. Koken, J.D. Embury, Scripta Metall. 38 (1988) 1045.

[43] N. Hansen, Mem. Sci. Rev. Met. 72 (1975) 189

[44] R. érsund, E. Nes, Scripta Metall. 22 (1988) 665.

[45] R. Ørsund, E. Nes, Scripta Metall. 22 (1988) 671

[46] D. Juul Jensen, N. Hansen, F.J. Humphreys, Acta Metall. 33(12) (1985) 2155.

[47] N. Hansen, B. Bay, Acta Metall. 29 (1981) 65.

[48] J. Hirsch, E. Nes, K. LuÈcke, Acta Metall. 35 (1987) 427.

[49] H. Mykura, in: Ballinffi (Ed.), Grain Boundary Structure and Kinetics, ASM, Ohio, OH, 1980, 445 pp.

[50] S. Dash, N. Brown, Acta Metall. 11 (1963) 1067.

[51] G. Gottstein, Acta Metall. 32 (1984) 1117

[52] P. Haasen, Met. Trans. A 24 (1993) 1001

[53] R.E. Fullman, J.C. Fisher, J. Appl. Phys. 22 (1951) 1350.

[54] G.F. Bolling, W.C. Wingard, Acta Metall. 6 (1957/1958) 283.

[55] K.T. Aust, J.W. Rutter, Trans. AIME 218 (1960) 50.

[56] K.T. Aust, J.W. Rutter, Trans. AIME 218 (1960) 682.

[57] K.T. Aust, J.W. Rutter, Trans. AIME 218 (1960) 1023

[58] A. Darsouni, B. Bouzabata and F. Montheillet, Hot Ductility of a Microalloyed Steel in the Intermediate Temperature Range, Colloque C7, supplCment au Journal de Physique 111, Volume 5, novembre 1995 C7-347

[59] S.L. Semiatin y G.D. Lahoti, *Metall. Trans. A* 13 (1982) 275-288

[60] C. García de Andrés, F.G. Caballero, C. Capdevila and L.F. Álvarez, Application of dilatometric analysis to the study of solid-solid phase transformations in steels, Department of Physical Metallurgy, Centro Nacional de Investigaciones Metalúrgicas (CENIM), Consejo Superior de Investigaciones Científicas (CSIC)

[61] F. Hairer, A. Karelova, C. Krempaseky, E. Wernerr, T. Hebesberger, A. Pichler, Etching techniques for the microstructural charectirization of complex phase steels by light microscopy.